# Characterization and Decomposition of the Natural van der Waals SnSb$_2$Te$_4$ under Compression

Juan A. Sans,* Rosario Vilaplana, E. Lora da Silva, Catalin Popescu, Vanesa P. Cuenca-Gotor, Adrián Andrada-Chacón, Javier Sánchez-Benitez, Oscar Gomis, André L. J. Pereira, Plácida Rodríguez-Hernández, Alfonso Muñoz, Dominik Daisenberger, Braulio García-Domene, Alfredo Segura, Daniel Errandonea, Ravhi S. Kumar, Oliver Oeckler, Philipp Urban, Julia Contreras-García, and Francisco J. Manjón

Read Online

ACCESS | Metrics & More | Article Recommendations | SI Supporting Information

**ABSTRACT:** High pressure X-ray diffraction, Raman scattering, and electrical measurements, together with theoretical calculations, which include the analysis of the topological electron density and electronic localization function, evidence the presence of an isostructural phase transition around 2 GPa, a Fermi resonance around 3.5 GPa, and a pressure-induced decomposition of SnSb$_2$Te$_4$ into the high-pressure phases of its parent binary compounds ($\alpha$-Sb$_2$Te$_3$ and SnTe) above 7 GPa. The internal polyhedral compressibility, the behavior of the Raman-active modes, the electrical behavior, and the nature of its different bonds under compression have been discussed and compared with their parent binary compounds and with related ternary materials. In this context, the Raman spectrum of SnSb$_2$Te$_4$ exhibits vibrational modes that are associated but forbidden in rocksalt-type SnTe; thus showing a novel way to experimentally observe the forbidden vibrational modes of some compounds. Here, some of the bonds are identified with metavalent bonding, which were already observed in their parent binary compounds. The behavior of SnSb$_2$Te$_4$ is framed within the extended orbital radii map of BA$_2$Te$_4$ compounds, so our results pave the way to understand the pressure behavior and stability ranges of other "natural van der Waals" compounds with similar stoichiometry.
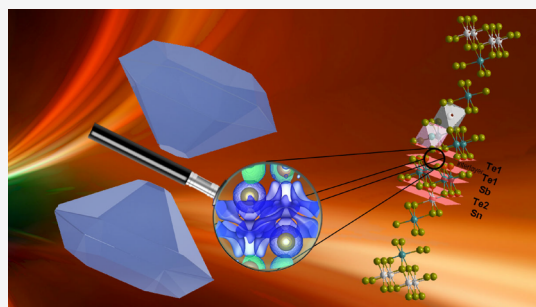
## 1. INTRODUCTION

The search for topological features in materials including topological insulators (TIs) and topological superconductors (TSs) is currently one of the hot topics in the material science field because of its relationship to fundamental physics and its applications in spintronics and quantum computation.[1−3] Recently, several tools have been designed to identify theoretically predicted TI candidates and create an extensive database of compounds that exhibit these properties,[4−6] defining respective limitations and filters required by theoretical calculations to avoid false-positive predictions.[7] The discovery of 3D-TI properties in layered tetradymite-like A$^{V}$$_2$X$^{VI}$$_3$ compounds, such as Bi$_2$Te$_3$, Bi$_2$Se$_3$, and Sb$_2$Te$_3$ compounds,[3,8,9] and the trivial insulating behavior of Sb$_2$Se$_3$[10] have opened the question about which is the electronic and structural origin and the limiting factors of this conduct, compared to other similar materials, such as the layered tetradymite-like B$^{IV}$A$^{V}$$_2$X$^{VI}$$_4$ compounds.

Binary A$_2$X$_3$ layered compounds are usually $p$-type semiconductors with a narrow gap, leading to a high electrical conductivity.[11] In particular, $\alpha$-Sb$_2$Te$_3$ and $\alpha$-Bi$_2$Te$_3$ are the best thermoelectric materials near room temperature found to

date,[12,13] since they feature a very small thermal conductivity. Additionally, the hybridization between the valence and the conduction band states favored by a large spin−orbit coupling (SOC) and a small bandgap, leads to the formation of Dirac cones in the electronic band structure that is responsible for their 3D-TI properties.[8] The TI properties observed in A$_2$X$_3$ binary compounds with layered tetradymite-like $R\bar{3}m$ structure [space group (s.g.) 166, Z = 3] have triggered the exploration of ternary BA$_2$X$_4$ compounds based on those materials.[8,14−16] These ternary compounds are expected to show richer physics than their binary counterparts, plus the possibility to tune their properties in a finer way by selecting appropriate B atoms. In fact, 3D-TI behavior has been predicted in many BA$_2$X$_4$ compounds,[11,14−19] and rhombohedral SnSb$_2$Te$_4$ with layered
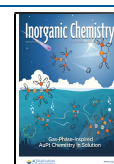
tetradymite-like structure has been found to be a *p*-type 3D-TI.[11]

The tetradymite-like structure of binary $A_2X_3$ compounds is a 2D layered structure formed by blocks composed by five layers (X1−A−X2−A−X1) and called *quintuple* layer (QL), with A and X being the cation and the anion, respectively, and X1 and X2 the two nonequivalent anions in the unit cell. These QLs pile up along the trigonal *c* axis and are traditionally considered to be linked by van der Waals (vdW) forces leading to the 3D material.[8]

In ternary $BA_2X_4$ compounds the tetradymite-like $R\bar{3}m$ structure is formed by replacing the central anion (X2) of $A_2X_3$ compounds with a three-atoms sub-block (X2−B−X2). In this way, the block is composed of seven layers (X1−A−X2−B−X2−A−X1) and called *septuple* layer (SL).[20] In these ternary compounds, the tetradymite-like structure can be described by two octahedra formed by A and B cations surrounded by six X1/X2 and X2 anions, respectively. In fact, these ternary compounds with tetradymite-like layered structure define a new family of materials, named "natural van der Waals heterostructures", whose nanosheets promise novel and interesting properties.[21]

Due to their technological interest, the thermoelectric properties of layered tetradymite-like $BA_2X_4$ compounds have been studied[21−25] and experimental results have shown that there is a certain disorder in the crystal structure.[17,26−31] In particular, $SnBi_2Te_4$ and $SnSb_2Te_4$ are the $BA_2X_4$ materials showing the smaller cation exchange in their atomic sites.[23,31,32] Noteworthy, some $BA_2X_4$ compounds, like rocksalt-type $SnSb_2Te_4$ and $GeSb_2Te_4$, have revealed strong properties as phase change materials since they are able to rapidly change between an amorphous and a crystalline state by light irradiation or current application. In particular, $SnSb_2Te_4$ crystallizes predominantly in the rhombohedral $R\bar{3}m$ structure (s.g. 166, Z = 3) while a smaller fraction crystallizes in the metastable rocksalt-type $Fm\bar{3}m$ structure (s.g. 225, Z = 4). Additionally, it can be stabilized in an amorphous phase with average octahedral coordination in the short-range order.[33] It must be stressed that both polymorphs of $SnSb_2Te_4$ (also $GeSb_2Te_4$) and its binary parent compounds, rhombohedral $R\bar{3}m$ $\alpha$-$Sb_2Te_3$ and rocksalt-type $Fm\bar{3}m$ SnTe (c-SnTe), do not accomplish the Lewis-octet rule. Consequently, some of them have been proposed to be incipient metals by showing the recently discovered metavalent bonding;[34−38] a matter still under debate.

High pressure (HP) studies have been conducted in rocksalt-type $SnSb_2Te_4$ and $GeSb_2Te_4$[39] and in rhombohedral $SnBi_2Te_4$.[40] A pressure-induced amorphization (PIA) was reported in rocksalt-type $SnSb_2Te_4$ ($GeSb_2Te_4$) upon compression above 11 (15) GPa,[39] whereas a pressure-induced electronic topological transition (ETT) has been suggested to occur in rhombohedral $SnBi_2Te_4$.[40] Despite these efforts, many questions have yet to be addressed for the rhombohedral $BA_2X_4$ compounds and in particular for $SnSb_2Te_4$, including its recently proposed superconducting character at HP.[41] For instance, "how does the presence of the new $SnTe_6$ octahedron in rhombohedral $SnSb_2Te_4$ affect the properties of the host $Sb_2Te_3$ structure?" and "how does rhombohedral $SnSb_2Te_4$ behave under compression?". In this scenario, we wonder if pressure on rhombohedral $SnSb_2Te_4$ leads to (i) a simple compression of the material remaining in the original structure; (ii) an isostructural phase transition (IPT) followed by a structural phase transition (PT) toward a different structure,

like in its parent compound $Sb_2Te_3$; (iii) an ETT, similar to its counterpart $SnBi_2Te_4$; (iii) a PIA, reported in rocksalt-type $SnSb_2Te_4$; or even (iv) a pressure-induced decomposition (PID).

In this work, we report the room-temperature structural, vibrational, and electrical properties of $SnSb_2Te_4$ under compression from an experimental and theoretical point of view by means of angle-dispersive X-ray diffraction (ADXRD), Raman scattering (RS) and transport measurements complemented with *ab initio* calculations and a thorough analysis of the electron density. We will show the good agreement between both experimental and theoretical descriptions and a comparison of the behavior of this material under compression with those that of its parent binary compounds ($\alpha$-$Sb_2Te_3$ and c-SnTe). We will pay special attention to the evolution of the interlayer vdW interaction under compression, considering this feature the key element to understand the behavior of the $c/a$ ratio under compression and the stability pressure range of its low-pressure (LP) phase. Moreover, we will demonstrate that $SnSb_2Te_4$ undergoes a pressure-induced IPT near 2 GPa followed by a PID above 7 GPa. The contextualization of this result on the framework of the ternary $BA_2X_4$ compounds can shed light on their behavior under compression. Finally, we will show that the RS of $SnSb_2Te_4$ and its comparison with the theoretical vibrational properties of $SnSb_2Te_4$ and those of its parent compounds has revealed that (i) there is a Fermi resonance around 3.5 GPa, similar to the one that occurs in c-SnTe, and (ii) the Raman spectrum of $SnSb_2Te_4$ shows some vibrational modes similar to those of forbidden c-SnTe. This result evidences a novel procedure to experimentally observe the forbidden vibrational modes of some materials. Finally, we will analyze the electronic topology of the different bonds found in $SnSb_2Te_4$ together with their evolution under pressure and show that this compound behaves like the recently proposed incipient metals.

## 2. EXPERIMENTAL DETAILS

Bulk samples were prepared by melting stoichiometric amounts of the pure elements Sn (99.999%, Smart Elements), Sb (99.999%, Smart Elements) and Te (99.999%, Alfa Aesar) at 950 °C for 93 h in sealed silica glass ampules under argon atmosphere and subsequent annealing at 450−500 °C for 2 days.[31] Representative parts of the samples were crushed to powders and fixed on Mylar foils with silicon grease to collect powder diffraction patterns on a Huber G670 powder diffractometer equipped with an imaging plate detector (Cu−K$\alpha_1$ radiation, Ge monochromator, $\lambda$ = 1.54051 Å) in Guinier geometry. Rietveld refinement of powder X-ray diffraction data confirmed the high purity of the samples.

HP-ADXRD measurements on $SnSb_2Te_4$ at 300 K using a membrane-type diamond-anvil cell (DAC) were carried out in experiment 1 (experiment 2) up to 37 GPa (12 GPa) in beamline I15 (MSPD beamline[42]) at Diamond Light Source synchrotron (ALBA synchrotron) using a monochromatic X-ray beam with $\lambda$ = 0.42408 Å ($\lambda$ = 0.4246 Å). In experiment 1 (experiment 2) images were collected using a MAR345 image plate (Rayonix MARCCD detector) located at 430 mm (240 mm) from the sample. In experiment 1 (experiment 2), $SnSb_2Te_4$ powder was loaded in a 150-$\mu$m diameter hole of a Rhenium (Inconel) gasket in a DAC with diamond-culet sizes of 350 $\mu$m using helium (silicone oil) as pressure transmitting medium (PTM). In both experiments, copper was placed inside the pressure cavity and used as the pressure sensor through copper EoS[43] and a pinhole placed before the sample position was used as a cleanup aperture for filtering out the tail of the X-ray beam, which was focused down to 20 × 20 $\mu$m$^2$ using Kickpatrick-Baez mirrors.

Diffraction patterns obtained in both experiments were integrated as a function of $2\theta$ using FIT2D software in order to give conventional, one-dimensional diffraction profiles.[44] The refinement of the powder diffraction patterns was performed using GSAS program package.[45,46] Due to the resonant excitation energy with Sn K-edge used in both experiments, the relative intensities are not accurate enough to perform Rietveld refinement but a Von Dreele-type Le Bail fit. The experimental structural parameters presented in this work have been obtained by means of a Von Dreele-type Le Bail method since the resonant excitation energy (Sn K-edge) used in both experiments avoided the obtaining of accurate relative intensities to perform Rietveld refinement.

Unpolarized HP-RS measurements up to 27 GPa using a membrane-type DAC and 16:3:1 methanol/ethanol/water mixture as PTM (quasi-hydrostatic up to 10 GPa),[47,48] were performed with a Horiba Jobin Yvon LabRAM UV HR microspectrometer equipped with a thermoelectrically cooled multichannel charge coupled device detector which allows a spectral resolution better than 2 cm$^{-1}$. The Raman signal was excited with a He−Ne laser (632.8 nm line) with a power of less than 10 mW and collected in backscattering geometry using an edge filter working in perpendicular configuration and cutting at 100 cm$^{-1}$. Raman signals down to 50 cm$^{-1}$ can eventually be detected by adjusting the angle between the edge filter and the light containing the Raman signal (provided that the Rayleigh signal is weak enough and the Raman signal is strong enough). Pressure was determined by the ruby luminescence method. The frequency of the Raman-active phonons has been experimentally analyzed by fitting Raman peaks with a Voigt profile fixing the Gaussian line width (1.6 cm$^{-1}$) to the experimental setup resolution.[51,52]

Electrical resistance of $SnSb_2Te_4$ under pressure was measured with the standard four-point probe van der Pauw method using 20 $\mu$m copper−beryllium wires. Single crystals of $SnSb_2Te_4$ of approximately 30 $\mu$m thick and 100 × 100 $\mu$m$^2$ surface were loaded into a Merrill-Bassett DAC with 400 $\mu$m culet diamonds. The electrical average resistance was measured by using four 20 $\mu$m copper−beryllium wires. Electrical resistance was measured under two different arrangements. In the first one, the sample was directly in contact with the anvils; i.e. under nonhydrostatic conditions. In the second one, the sample was inside a stainless steel gasket and surrounded by CsI powder as PTM; i.e. under quasi-hydrostatic conditions. Electrical resistance showed similar trends in both arrangements, likely due to the anisotropic (layered) and soft nature of the crystals. Luminescence lines of ruby powder were used to calibrate the pressure inside the cavity in both methods.[49,50]

## 3. THEORETICAL CALCULATIONS

*Ab-initio* calculations have been performed within the density functional theory (DFT)[53] using plane-wave basis-sets and the projector-augmented wave (PAW)[54] scheme with the Vienna *ab-initio* simulation package (VASP) package.[55] Calculations of the electronic-band structures have been considered by employing spin−orbit coupling (SOC). The plane-wave kinetic-energy cutoff was defined with 320 eV, in order to achieve highly converged results. We have used the generalized-gradient approximation (GGA) for the exchange-correlation energy with the Perdew−Burke−Ernzerhof para-metrization revised for solids (PBEsol).[56] At each selected volume, the structures were fully relaxed to their equilibrium configuration through the calculation of the forces on atoms and the stress tensor with a dense special $k$-point sampling Monkhorst−Pack grids. In particular, the electronic band structures along high-symmetry directions and the correspond-ing electronic density of states (EDOS) were computed with a mesh of 18 × 18 × 18 $k$-points. The application of DFT-based calculations to the study of semiconductor properties under HP has been reviewed in the literature.[57]

Lattice-dynamics calculations of phonon modes were performed at the zone center ($\Gamma$ point) of the Brillouin zone. For the calculation of the dynamical matrix at $\Gamma$ we used the direct force-constant approach (or supercell method),[55,58] which involves the calculation of all the atomic forces when each nonsymmetry related atom in the unit cell is displaced along nonsymmetry related directions.

The Bader analysis was performed by partitioning the PBEsol-DFT core and valence charge density grids.[59−63] A fine FFT grid was required to accurately reproduce the correct total core charge. The non-covalent interactions (NCI) of the PBEsol-DFT charge densities was computed using the NCI index.[64,65] Such a tool defines a visualization index based on the electron density and its derivatives, enabling identification of noncovalent interactions, based on the peaks that appear in the reduced density gradient at low densities.

## 4. RESULTS AND DISCUSSION

**4.1. X-ray Diffraction under Pressure.** *4.1.1. LP Phase.* As already commented, $SnSb_2Te_4$ usually crystallizes in a rhombohedral $R\overline{3}m$ polymorph following a $GeSb_2Te_4$ structure-type with four atoms at the independent Wyckoff sites (Sn at 3a and Sb, Te1, and Te2 at 6c). A clear scheme of the polyhedral arrangement for the $GeSb_2Te_4$-type structure is shown in Figure 1, together with a description of the different layers composing this compound. The Von Dreele-type Le Bail fit of the experimental XRD pattern at room conditions (see Figure S1) yields a trigonal unit-cell volume of 662.7(7) Å$^3$ with lattice parameters $a = 4.2977(1)$ Å and $c = 41.43(4)$ Å.
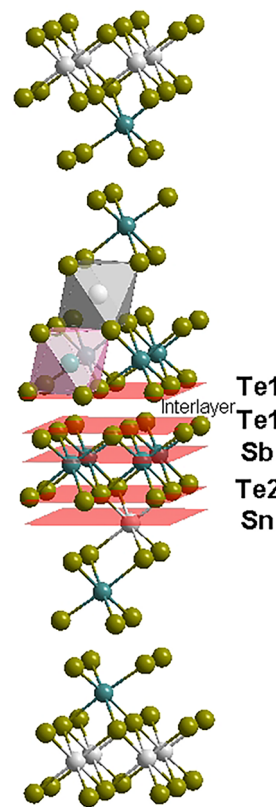


**Figure 1.** 3D structure layout of the $SnSb_2Te_4$ compound. Atomic planes are defined, including an additional Te1 plane to define the interlayer section.

These values are in good agreement with those reported in the literature and obtained from theoretical simulations (see Table 1).

### Table 1. Calculated (th.) and Experimental (exp.) Volume ($V_0$), Bulk Modulus ($B_0$), and Its Derivative ($B_0'$) of $SnBi_2Te_4$ and $SnSb_2Te_4$ at Ambient Pressure

|  | $V_0$ (Å³) | $B_0$ (GPa) | $B_0'$ |
|---|---|---|---|
| **$SnSb_2Te_4$** |  |  |  |
| exp.[a] | 663.1(6) | 31.6(14) | 8(8) |
| th.(GGA-PBESol)[b] | 659.3(6) | 41.0(15) | 6.5(6) |
| **$\alpha$-$Sb_2Te_3$** |  |  |  |
| exp.[c] | 481.1(8) | 36.1(9) | 6.2(4) |
| th.(GGA-PBESol)[d] | 473.1(8) | 43(2) | 4.3(5) |

[a]This work. [b]Calculations from the literature including SOC in this work. [c]Average experimental value.[41] [d]Calculations including SOC.[41]

Two ADXRD experiments were carried out by employing helium (up to 37 GPa) and silicone oil (up to 12 GPa) as a pressure-transmitting medium (PTM). The latter experiment up to 12 GPa (experiment 2) was performed in order to conduct a more detailed study of the LP phase. ADXRD patterns of $SnSb_2Te_4$ at different pressures from experiment 2 are shown in Figure S1.

In Figure S1 it is possible to observe a clear shift of the Bragg reflections of the LP phase of $SnSb_2Te_4$ toward higher $2\theta$ angles with increasing pressure. This feature occurs due to the monotonous decrease of the distances between crystallographic planes with compression. A clear change in the diffraction patterns above 7 GPa suggests that the LP phase is no longer stable. We want to stress here that the lack of Rietveld refinement of our measurements prevents us from obtaining the experimental atomic positions in $SnSb_2Te_4$. Consequently, we have used the atomic positions of our calculations to discuss the pressure dependence of many parameters in order to understand the behavior of $SnSb_2Te_4$ under compression. The good agreement between the experimental and theoretical pressure dependence of the unit cell volume, lattice parameters, and the $c/a$ ratio discussed in the following paragraphs assures us of the accuracy of our theoretical data for further considerations.
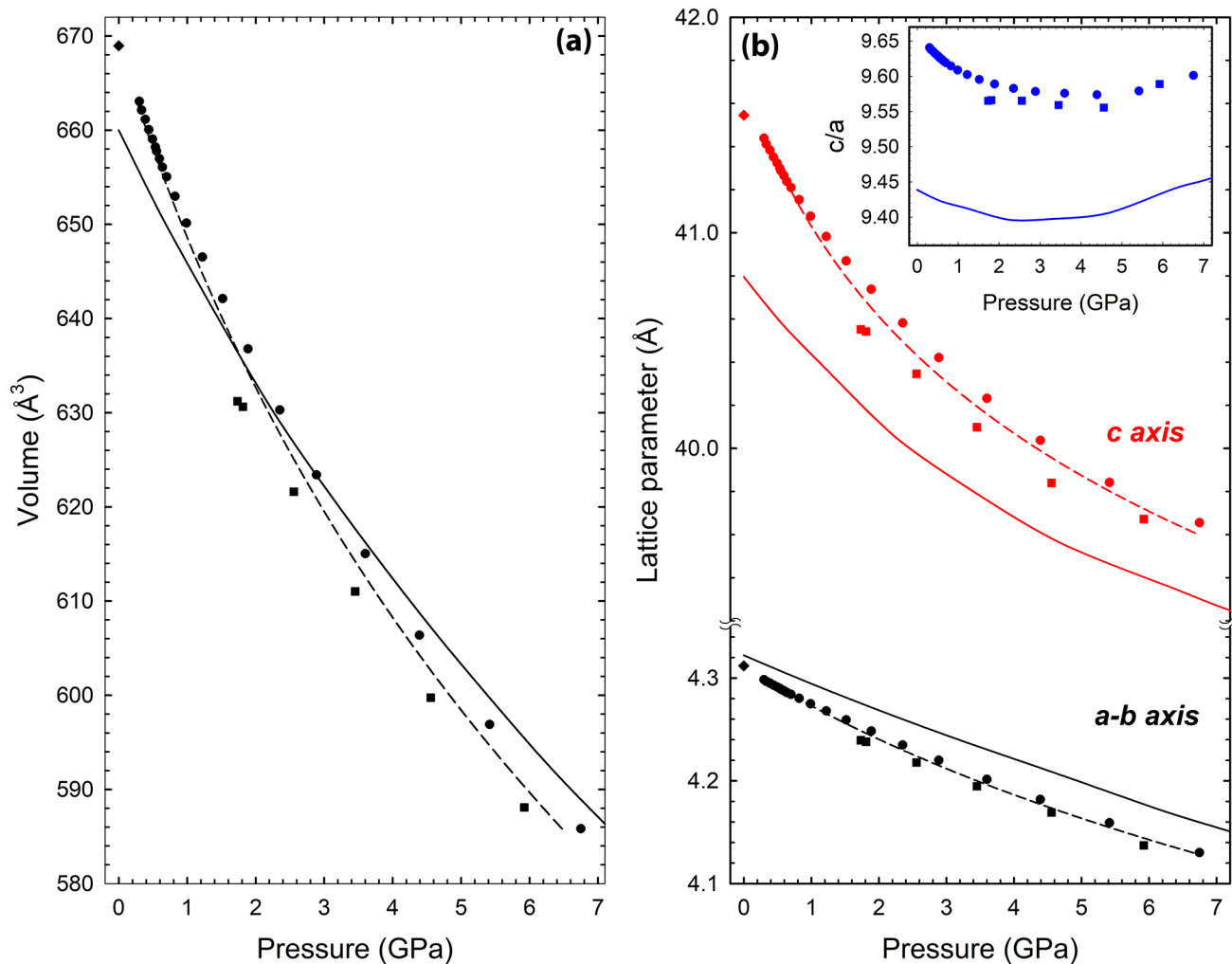


**Figure 2.** Pressure dependence of the unit cell volume (a) and lattice parameters (b). The inset shows the evolution of the $c/a$ ratio with pressure. Solid lines represent the theoretically simulated data, dashed lines represent the fit to EoS equations, solid circles are the experimental data obtained using silicone oil as PTM, and solid squares are the experimental data obtained using helium as PTM. Diamond solid circles belong to values obtained from literature (ref. 31).

**Table 2. Calculated (th.) and Experimental (exp.) Lattice Parameters of SnBi$_2$Te$_4$ and SnSb$_2$Te$_4$ and Their Associated Axial Compressibilities**

| | $B_{0a}$ (GPa) | $B_{0c}$ (GPa) | $\kappa_a$ ($10^{-3}$ GPa$^{-1}$) | $\kappa_c$ ($10^{-3}$ GPa$^{-1}$) |
|---|---|---|---|---|
| SnSb$_2$Te$_4$ | | | | |
| exp.[a] | 42.4(2) | 23.8(4) | 7.9(3) | 14(2) |
| th. (GGA-PBESol)[b] | 48(2) | 30(4) | 6.9(7) | 11.1(15) |
| $\alpha$-Sb$_2$Te$_3$ | | | | |
| exp.[c] | 47.3(12) | 22(3) | 7.0(2) | 15.0(5) |
| th. (GGA-PBESol)[b] | 48(1) | 21(2) | 6.94(14) | 15.9(7) |
| SnBi$_2$Te$_4$ | | | | |
| exp.[d] | 42.3(17) | 25.3(17) | 7.9(3) | 13.1(9) |
| th. (GGA-PBESol)[d] | 48.0(15) | 30(2) | 6.9(7) | 11.1(7) |

[a]This work. [b]Calculations including SOC in this work. [c]Calculated from data from literature.[41,97] [d]Data from the literature,[37] where calculations include SOC.

The pressure dependence of the experimental and theoretical unit cell volume and lattice parameters of SnSb$_2$Te$_4$ of the two experiments is displayed in parts a and b of Figure 2, respectively. The slight discrepancy observed in both figures between the values obtained using helium and silicone oil as PTM can be explained by the typical pressure uncertainty in these experiments (~0.5 GPa). The experimental unit cell volume (of both experiments) was fitted to a third-order Birch–Murnaghan equation of state (BM-EoS) with a $B_0'$ higher than 4, as suggested by the positive trend of the $F-f$ plot calculated from EoSFIT.[66] The experimental BM-EoS (see Figure 2a) yields a zero-pressure unit cell volume, $V_0$, and bulk modulus, $B_0$, of 663.1(6) Å$^3$ and 31.6(4) GPa, respectively. These values are in good agreement with our calculations (see Table 1).

The similar features of the layered structure of SnSb$_2$Te$_4$ and its parent binary compound $\alpha$-Sb$_2$Te$_3$ suggest that the compressibility of the former must be related to that of the latter. More precisely, the compression of the former should be a combination of the compression of the SbTe$_6$ polyhedral units, also present in $\alpha$-Sb$_2$Te$_3$, and of the SnTe$_6$ polyhedral units (a quasi-regular SnTe$_6$ octahedron) in the center of the SL, also present in c-SnTe compound. This hypothesis is supported by the similar volume compressibility of both SnTe$_6$ and SbTe$_6$ octahedral units in SnSb$_2$Te$_4$ and those occurring in its two parent binary compounds as shown in Figure S2.

The evolution of the theoretical interatomic distances of SnSb$_2$Te$_4$ at HP (Figure S3) shows that the Sn–Te interatomic distance inside the quasi-regular SnTe$_6$ octahedron compresses at a similar rate as the Sn–Te distances in c-SnTe ($B_0 \approx 50$ GPa).[67] Since the Sn–Te distance is the second less compressible interatomic distance of the SnSb$_2$Te$_4$ structure, it can be assumed that the compressibility of SnSb$_2$Te$_4$ is mostly determined by the compressibility of $\alpha$-Sb$_2$Te$_3$. This hypothesis is confirmed by both experimental and theoretical data, shown in Table 1. Note that $\alpha$-Sb$_2$Te$_3$ shows an experimental average $B_0$ of 36.1(9) GPa[68] that is in very good agreement with the experimental bulk modulus of SnSb$_2$Te$_4$. In conclusion, the compressibility of SnSb$_2$Te$_4$ is dominated by the $\alpha$-Sb$_2$Te$_3$ component due to the harder behavior of the intercalated SnTe$_6$ octahedron.

The experimental $B_0$ of SnSb$_2$Te$_4$ is similar to that of the isostructural compound SnBi$_2$Te$_4$ ($B_0$ = 35(2) GPa).[40] This result implies that the compressibility of these two layered BA$_2$X$_4$ compounds is almost independent of the A cation and fully dependent on geometrical factors of the layered structure. A close look at the pressure dependence of the theoretical

interatomic distances in Figure S3 shows a much larger compression of the Te1–Te1 interlayer distance than that found for the Sn–Te and Sb–Te intralayer distances. Therefore, the bulk compressibility of SnSb$_2$Te$_4$ (also for SnBi$_2$Te$_4$) is dominated by the compressibility of the vdW gap between the SLs. The compressibility of the Te1–Te1 interlayer distance is similar for both SnSb$_2$Te$_4$ and $\alpha$-Sb$_2$Te$_3$, in good agreement with the similar bulk compressibilities of both compounds, shown in Table 1. In conclusion, the compressibility of SnSb$_2$Te$_4$ is dominated by the strong compression of the Te–Te interlayer distance, assumed to be mostly governed by the vdW interactions, and consequently is similar to that of $\alpha$-Sb$_2$Te$_3$ and SnBi$_2$Te$_4$.

Regarding the evolution of the experimental and theoretical lattice parameters at HP (see Figure 2b), they can be fitted to a modified BM-EoS in order to reproduce their sublinear behavior. Table 2 summarizes the axial bulk modulus, $B_{0i}$, and the axial compressibility as $\kappa_i = \frac{1}{3B_{0i}}$ obtained for each lattice parameter. At room conditions, $\kappa_c \sim 2\kappa_a$ is consistent with the much larger compression of the Te1–Te1 interlayer distance along the $c$-axis than the Sn–Te and Sb–Te intralayer distances in the $a-b$ plane (Figure S3). Such a hypothesis is further substantiated by the evolution of the different interplanar distances along the $c$-axis (see Figure S4), which allows us to identify the different contributions to the compressibility of the $c$-axis. The strong reduction of the interplanar compressed Te1–Te1 distance when compared with the behavior of the overall interplanar distances corroborates that the Te1–Te1 interplanar distance dominates the compression along the $c$-axis. Moreover, a fit of the interplanar Te1–Te1 distance with a modified BM-EoS yields a bulk modulus of 21(1) GPa that is similar to that of the $c$-axis (23.8(4) GPa). Therefore, we can conclude that the interplanar Te1–Te1 distance, assumed to be determined by the vdW interaction, is the main source for the compressibility of the unit cell along the $c$-axis and that the stronger reduction of the Te1–Te1 distance than the Sb–Te1 or Sb–Te2 distance is also the responsible for the much larger compressibility along the $c$-axis than along the $a$-axis.

Additional support to the interpretation provided in the previous paragraph is obtained by comparing the experimental and theoretical $B_{0i}$ and $\kappa_i$ of SnSb$_2$Te$_4$ with those of SnBi$_2$Te$_4$[40] and $\alpha$-Sb$_2$Te$_3$[68,69] presented in Table 2. The close similarity of the values of the $B_{0i}$ and $\kappa_i$ in the three compounds supports the presence of similar mechanisms of compression and a similar strength of the interatomic interactions in all of them.

It is noteworthy of mentioning that the compression of the $c$-axis in $SnSb_2Te_4$ does not imply a compression of all the interplanar distances along the $c$-axis. Despite the decrease of the Sb−Te1 interatomic distance for $SnSb_2Te_4$ (see Figure S3), the interplanar Sb−Te1 distance expands under compression, and the same occurs for $\alpha$-$Sb_2Te_3$ (see Figure S4). This feature clearly suggests an increase of the angle between the $a$−$b$ plane and the Sb−Te1 bond at HP that distorts the $SbTe_6$ octahedron as clearly observed in Figure S5a. We also intend to highlight that although the Sb−Te1 interatomic distance shows the same pressure dependence in $SnSb_2Te_4$ and $\alpha$-$Sb_2Te_3$, the presence of the short Sn−Te bond in $SnSb_2Te_4$ triggers a slight increase of the Sb−Te2 interatomic distance, and a consequent larger decrease of the Sn−Te bond with pressure than in c-SnTe. This result means that there is a slightly larger and weaker Sb−Te2 bond in $SnSb_2Te_4$ than in $\alpha$-$Sb_2Te_3$. This variation caused by the chemical pressure induced by the combination of the binary parent compounds (c-SnTe and $\alpha$-$Sb_2Te_3$) in the formation of $SnSb_2Te_4$, can also be understood through the change in the orientation of the lone electron pair (LEP) of Sb, which can induce a slight distortion of the $SbTe_6$ polyhedral unit. This distortion is small because the compressibility of the Sb−Te2 interatomic distance for both $SnSb_2Te_4$ and $\alpha$-$Sb_2Te_3$ compounds follows a similar pattern.

A good agreement between experimental and theoretical data is also found for the evolution of the $c/a$ ratio at HP (see the inset of Figure 2b). This ratio shows a clear change of tendency above 2 GPa similar to that observed in $\alpha$-$Sb_2Te_3$[68,69] and $SnBi_2Te_4$.[40] The minimum of the $c/a$ ratio in $SnSb_2Te_4$ can also be explained by analyzing the pressure dependence of respective interplanar distances along the $c$-axis (see Figure S4). In particular, the evolution of the Te1−Te1 interplanar distance in $SnSb_2Te_4$ shows a strong (normal) compression below (above) 2 GPa. This behavior is typically associated with the weak character of the vdW bonds at LP and its hardening due to the increase of the covalent character of the Te−Te bonds at HP.[70] A similar behavior of the $c/a$ ratio is observed for $\alpha$-$Sb_2Te_3$ since the Sb−Te interplanar distances evolve in this compound in a similar manner as in $SnSb_2Te_4$ (see Figure S4). Therefore, we can conclude that the change of the compression rate of the interlayer space (caused by the change of the compressibility of the Te1−Te1 interplanar distance) gives rise to the $c/a$ ratio minimum observed in $SnSb_2Te_4$ and $\alpha$-$Sb_2Te_3$. The evolution of the vdW character of the interlayer bonds at HP will be addressed in depth later on, when we discuss the analysis regarding the dependence of the electronic topology at HP.

The big change in the slope of the $c/a$ ratio in $SnSb_2Te_4$ and related compounds at HP is likely related to a pressure-induced IPT. We must recall that these chalcogenides are mainly composed by group-15 cations acting with their lowest valence state and featuring a strong cationic LEP stereoactivity that has a deep effect in the formation of the 2D layered structure. The presence of the cationic LEP can modify the electronic distribution of the charges in the crystal and distorts the geometry of the bonds. Moreover, the cationic LEP is mainly oriented along the $c$-axis in these compounds and contributes to the vdW interaction between the layers and to the strong compressibility of the $c$-axis at LP since the LEP is extremely compressible at LP. This scenario has been already observed in a number of group-15 sesquichalcogenides.[71,72] Additionally, it has been widely reported that both the cationic LEP and the

vdW interaction become more incompressible at HP due to the progressive decrease of the LEP stereoactivity and the increase of the strength of the interlayer forces. The changes in compressibility of electronic "density-clouds" at relatively LP lead to a new isostructural phase with a different $c/a$ ratio in $SnSb_2Te_4$ and related chalcogenides, and these can be understood as an IPT of electronic origin, as we will further show.

A different way of understanding the structural behavior of $SnSb_2Te_4$ at HP is by studying the compression of the two octahedral units forming the $SnSb_2Te_4$ heterostructure: the regular octahedron around Sn and the slightly deformed octahedron around Sb (see Figure 1). Figure S6 shows the evolution of the theoretical quadratic elongation of both octahedra at HP. This parameter was defined by Robinson et al.[73] to analyze the distance of the inner atom of a polyhedron with respect to the central position, which is an indirect measurement of the irregularity of the polyhedral unit. In our case, the $SnTe_6$ ($SbTe_6$) octahedron shows practically no changes in the quadratic elongation up to 2 GPa and an increase above 2 (4) GPa. This result suggests that both octahedra are almost insensitive to pressure while there is a strong compression of the vdW interlayer gap below 2 GPa. Nevertheless, $SnTe_6$ octahedra show a considerable increase of the polyhedral distortion above 2 GPa; once the vdW gap becomes as incompressible as the octahedral units. Therefore, results of Figures S5 and S6 support the occurrence of a pressure-induced IPT near 2 GPa in $SnSb_2Te_4$.

Finally, in order to measure the differences of the interatomic distances in both octahedra with respect to those in a regular coordination, we have plotted in Figure S7 the evolution of the theoretical distortion index of both octahedra at HP.[74] It can be observed that the regular $SnTe_6$ octahedron remains regular during the whole compression process while the distorted $SbTe_6$ octahedron becomes slightly more regular under compression. This is a consequence of the evolution of the Sb−Te1 and Sb−Te2 distances under compression, which tend to follow a similar pattern, but at a different rate. In summary, we have shown that the very definition of the $SnSb_2Te_4$ heterostructure as a layered distribution of SLs makes it essential to analyze the polyhedral units and the inter- and intralayer compressibility in order to understand their respective behavior at HP.

To close this section, we have plotted the experimental quadratic elongations of the $AX_6$ and $BX_6$ octahedra of all known $BA_2X_4$ compounds in order to have the $R\bar{3}m$ structure at room pressure according to the ICSD database (see Figure 3). In this way, we can try to shed light on the HP behavior of the compounds of this ternary family. It can be observed that $SnSb_2Te_4$ is one of the compounds with the smallest quadratic elongation of the $AX_6$ octahedron ($SbTe_6$) and conversely with the largest quadratic elongation of the $BX_6$ octahedron ($SnTe_6$). Therefore, according to the trend observed in the theoretical quadratic elongation of both octahedra at HP (see Figure S6), it can be deduced that $SnSb_2Te_4$ will behave at HP similarly to $PbSb_2Te_4$ at LP, while $SnBi_2Te_4$ tends to behave at HP as $GeSb_2Te_4$ at LP.

Regarding the Figure 3, more conclusions can be drawn. *A priori*, it could be thought that the $AX_6$ quadratic elongation should increase in the sequence As−Sb−Bi due to the larger stereoactivity of the LEP in As than in Sb and Bi. This fact is due to the stronger hybridization of the cationic s−p levels in As than in Sb and Bi for a given atom.[75] On the other hand, it
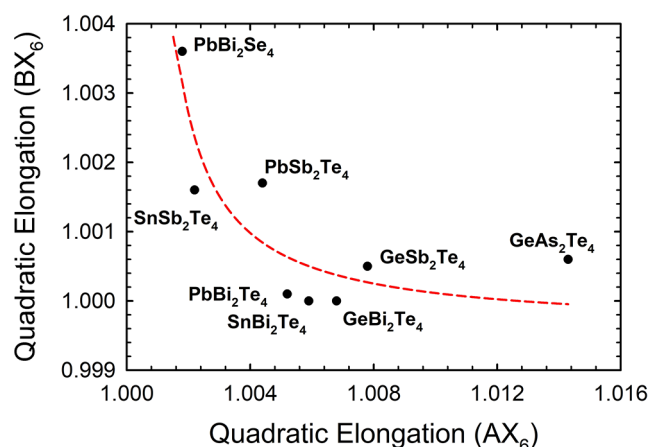
**Figure 3.** Relationship between the quadratic elongation of the $BX_6$ octahedron and the quadratic elongation of the $AX_6$ octahedron in $AB_2X_4$ materials. Structural data were obtained from refs 27, 28, and 130−136.

could also be thought that the $BX_6$ quadratic elongation should increase in the sequence Pb−Sn−Ge due to the larger difference between the s−p levels in Pb than in Sn and Ge.[75] Unexpectedly, the above arguments seem not to be true since $SnBi_2Te_4$ (with a common B cation with $SnSb_2Te_4$) has a larger $AX_6$ quadratic elongation, whereas $GeSb_2Te_4$ (with a common A cation with $SnSb_2Te_4$) has a smaller $BX_6$ quadratic elongation and a much larger $AX_6$ quadratic elongation. Therefore, results of Figure 3 suggest that there is a close relationship between the quadratic elongation of the $AX_6$ and $BX_6$ octahedra in these compounds and that not all combinations of $AX_6$ and $BX_6$ quadratic elongations are compatible with the $R\overline{3}m$ structure. This hypothesis is supported by the lack of compounds $PbAs_2Te_4$ and $SnAs_2Te_4$ with $R\overline{3}m$ structure, which should be located in the upper right region in the diagram; i.e., far away from the red line marking the average of the possible $AX_6$ and $BX_6$ quadratic elongations. A similar reasoning can be applied to explain why $PbSb_2Se_4$, $SnSb_2Se_4$, $PbBi_2S_4$, and $SnSb_2S_4$ cannot crystallize in the $R\overline{3}m$ structure.[76−78] In this context, it must be recalled that the LEP stereoactivity of group 15 cations increases when the anion follows the sequence Te−Se−S−O.[75] Therefore, taking into account the energetic difference between the p-levels of the anion and the s-levels of the cation, the strong LEP stereoactivity of As in tellurides should be similar to that of Sb cation in selenides and sulfides and to that of Bi in sulfides and oxides. Consequently, this strong cation LEP stereoactivity allows us to explain why the above-mentioned compounds do not crystallize in the $R\overline{3}m$ phase.

A different interpretation of the distortion of the $AX_6$ and $BX_6$ octahedra, but compatible with the LEP influence, can be the existence of a Peierls distortion,[79,80] which has been studied in several chalcogenides.[27] This periodic distortion in the crystalline lattice is associated with a charge density wave order and Fermi surface nesting. However, in the literature, a strong controversy has arisen between these two competitive effects (s-p mixing that enhances the LEP effect and the Peierls distortion). While the structural distortion observed in pure group 15 elemental structures, such as P (black phosphorus) and As has been associated with the influence of the LEP, it cannot be rule out that the Peierls distortion could be the dominating factor in the structure of Sb and Bi.[81] On the other

hand, the literature proposes the impossibility to form the nesting of the Fermi surface (origin of the Peierls lattice distortion) near the circular Dirac cone in TIs compounds such as $SnSb_2Te_4$.[82] However, charge density wave order has been found in a weak TI compound as Sb $(111)$[83] and more recently in $Bi_2Se_3$ (thought to be caused by interstitial Bi atoms between the QLs).[84] In fact, the most extended theory is that both LEP and Peierls distortion can coexist and be both the source of the irregularity of the $SbTe_6$ octahedron.[85] These last studies open the possibility that cation disorder in $SnSb_2Te_4$ along the c-axis could lead to the presence of interstitial atoms between the layers and could lead to a 1D Peierls distortion affecting the $SbTe_6$ units. Further studies are required to discern the origin of the polyhedral distortion in these systems.

*4.1.2. Pressure-Induced Decomposition (PID).* Above 7 GPa, a clear change of the experimental XRD patterns occurs. The disappearance of Bragg reflections around 11.0 and 14.6 degrees and the appearance of new peaks at 8.6 and 10.1 degrees (at 10.8 GPa) without showing a relevant peak broadening suggests the absence of a PIA. Thus, the only two possibilities are a PT or a PID.

In order to probe possible crystalline HP phases after a PT, we have resorted to the structure field map of $BA_2Te_4$ compounds reported by Zhang et al.,[86] with ternary compounds systematically ordered according to the cationic orbital radii, $R_B$ and $R_A$.[87] This structure field map (see Figure 4) allows us to understand and predict the structures of ternary
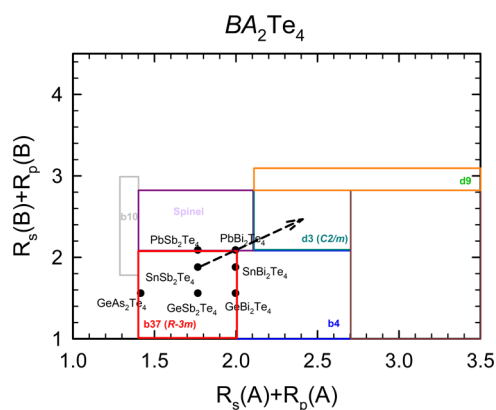


**Figure 4.** Updated orbital radii map of stable $BA_2Te_4$ compounds initially proposed by Zhang et al.[76]

$BA_2Te_4$ compounds at LP by knowing $R_B$ and $R_A$. Moreover, it can help in predicting the HP phases if we know how orbital radii behave at HP. In the field map of Zhang et al., materials with $R_B \in [1.6, 1.9]$ au and $R_A \in [1.0, 2.0]$ au crystallize in the b37 structure (s.g. $R\overline{3}m$); however, new tellurium-based ternary chalcogenides formed by different group 14 B cations (B = Ge, Sn and Pb) group 15 A cations (A = As, Sb and Bi) also crystallize in s.g. $R\overline{3}m$ according to the ICSD database. These are the cases of $GeAs_2Te_4$ (with $R_B = 1.415$ au and $R_A = 1.560$ au) and $PbBi_2Te_4$ (with $R_B = 1.997$ au and $R_A = 2.090$ au). We have included these two compounds in the structure field map because they limit the new borders of materials with s.g. $R\overline{3}m$. In this way, we can extend the stability ranges of the b37 structure to $R_B \in [1.4, 2.0]$ au and $R_A \in [1.0, 2.1]$ au with respect to the structure field map reported by Zhang et al.[87]

The new structure field map of $BA_2Te_4$ compounds allows us to consider several possible HP phases for a compound with

an initial $R\bar{3}m$ structure. The most important ones are the spinel b4 structure (s.g. $P\bar{4}2m$ or $I\bar{4}$) and the monoclinic d3 structure (s.g. $C2/m$). It is noteworthy to highlight that one of the parent binary compounds of $SnSb_2Te_4$ ($\alpha$-$Sb_2Te_3$) has the $R\bar{3}m$ structure and undergoes a PT toward a $C2/m$ structure ($\beta$-$Sb_2Te_3$).[88] Therefore, the latter phase could be a good candidate for the ternary compound $SnSb_2Te_4$ to crystallize in. The same reasoning applies to $SnBi_2Te_4$ since $\alpha$-$Bi_2Te_3$ also has the $R\bar{3}m$ structure and undergoes a PT toward a $C2/m$ structure ($\beta$-$Bi_2Te_3$).[88] Nevertheless, all our attempts to experimentally identify the possible HP phase with the help of theoretical simulations failed.

Subsequently, we have considered the possibility of a PID. For this purpose, we have calculated the formation enthalpy of $SnSb_2Te_4$ in s.g. $R\bar{3}m$ and compared it with those of the HP phases of its binary compounds (Figure 5). We have found
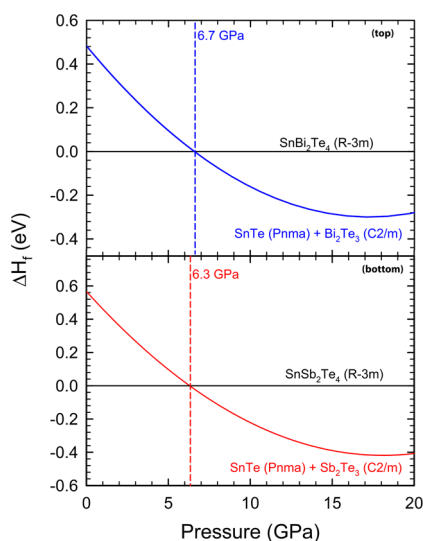


**Figure 5.** Relative formation enthalpy of the HP phases of the parent binary compounds with respect to the $R\bar{3}m$ structure of $SnSb_2Te_4$ and $SnBi_2Te_4$.

that above 6.3 GPa the combination of the HP phases $\beta$-SnTe (s.g. $Pnma$) and $\beta$-$Sb_2Te_3$ (s.g. $C2/m$) is energetically more favorable than the LP phase of $SnSb_2Te_4$. This result suggests that the ternary compound $SnSb_2Te_4$ should decompose into their parent binary materials above 6.3 GPa. In fact, we have found that the ADXRD patterns observed above 7 GPa in $SnSb_2Te_4$ (Figure S1) exhibit a perfect fit with the HP phases

of the binary parent compounds. A similar theoretical result has been obtained for $SnBi_2Te_4$ (see Figure 5), thus suggesting that also PID should be observed in $SnBi_2Te_4$ above 7 GPa.

It must be stressed that PID is not a common phenomenon occurring at room temperature, unlike PIA. In fact, similar compounds like $Ge_2Sb_2Te_5$ undergo PIA at room temperature.[89] The PIA at room temperature is mainly due to the frustration of either a PT to a HP phase or a PID into daughter compounds.[90] This frustration mainly occurs due to kinetic features governed by temperature. In fact, PID is usually observed in complex compounds mostly at high temperature[91−94] or in some molecular materials, such as $H_2S$, where PID occurs at room temperature and at very HP.[95] $SnSb_2Te_4$ is one of the few compounds exhibiting PID at room temperature and relatively LP (7 GPa). This result might be related to the large stability of their polyhedral units that prevail after the PID.

We want to finish by pointing out that the PID of rhombohedral $SnSb_2Te_4$ into their binary compounds may explain the superconducting properties recently proposed for this material above 8 GPa,[41] since $\beta$-$Sb_2Te_3$ exhibits a similar superconducting character around the same pressure.[96] Thus, $\beta$-$Sb_2Te_3$ may be responsible for the superconducting properties associated with $SnSb_2Te_4$.[97]

**4.2. Raman Scattering Measurements under Pressure.** In order to corroborate the results found in the structural study under pressure, we performed unpolarized HP-RS measurements. Since there is one formula unit (7 atoms) in the primitive unit cell of $SnSb_2Te_4$, this compound has twenty-one normal vibrational modes at $\Gamma$ with the following mechanical decomposition:[98]

$$\Gamma = 3A_{1g}(R) + 3A_{2u}(IR) + 3E_u(IR) + 3E_g(R) + A_{2u} + E_u$$

where E modes are doubly degenerated, $A_{1g}$ and $E_g$ modes are Raman-active (R), and $A_{2u}$ and $E_u$ are IR-active except for one $A_{2u}$ and one $E_u$ mode that correspond to the three acoustic phonons, considering that E-type modes are doubly degenerated. Therefore, there are six Raman-active modes ($\Gamma_{Raman} = 3A_{1g} + 3E_g$) and six IR-active modes ($\Gamma_{IR} = 3A_{2u} + 3E_u$). The assignment of the vibrational modes to atomic movements was done through the Jmol Interface for Crystallographic and Electronic Properties (J-ICE)[99] and is discussed in the Supporting Information (see Figures S8−S17).

Figure S18 shows the unpolarized RS spectrum of $SnSb_2Te_4$ at room conditions together with the position of the

**Table 3. Theoretical and Experimental Raman-Active Mode Frequencies and Their Pressure Coefficients of $SnSb_2Te_4$ at Room Temperature as Fitted with the Equation $\omega(P) = \omega_0 + aP + bP^2$ Compared with Those of Theoretically Simulated $\alpha$-$Sb_2Te_3$**

| | SnSb₂Te₄ | | | | | | α-Sb₂Te₃ | | |
| | experiment | | | theoretical calculations[a] | | | theoretical calculations[a] | | |
| mode symmetry | $\omega_0$ (cm⁻¹) | $a$ (cm⁻¹/GPa) | $b$ (cm⁻¹/GPa²) | $\omega_0$ (cm⁻¹) | $a$ (cm⁻¹/GPa) | $b$ (cm⁻¹/GPa²) | $\omega_0$ (cm⁻¹) | $a$ (cm⁻¹/GPa) | $b$ (cm⁻¹/GPa²) |
|---|---|---|---|---|---|---|---|---|---|
| $E_g^1$ | – | – | – | 38.87(15) | 2.52(8) | −0.081(9) | 50.4 | 2.62 | −0.09 |
| $A_{2g}^1$ | 53.3(8) | 4.2(6) | −0.15(8) | 55.3(2) | 4.25(12) | −0.145(12) | 68.9 | 4.3 | −0.07 |
| $E_g^2$ | 103.3(4) | 3.7(7) | −0.4(2) | 100.51(8) | 2.45(6) | – | 116.6 | 2.11 | |
| $A_{2g}^2$ | 107.8(14) | 4.6(6) | −0.15(6) | 115.1(2) | 2.70(18) | – | 167.6 | 2.57 | |
| $E_g^3$ | – | – | – | 116.65(17) | 4.63(13) | – | | | |
| $A_{2g}^3$ | 160.87(14) | 2.68(11) | −0.035(15) | 167.10(16) | 3.38(8) | −0.041(9) | | | |

[a]This work

theoretically predicted frequencies at these conditions (see vertical bottom tick marks). The RS spectrum at room conditions shows five of the six theoretically predicted Raman-active modes. A rather good agreement between the experimental and theoretical Raman-active mode frequencies at room pressure is observed (see also Table 3). Consequently, we have made a tentative assignment of experimental Raman modes considering the predicted frequencies and pressure coefficients as discussed below.

It is well-known that in layered materials vibrational modes at the Γ point can be classified into interlayer modes (in the low-frequency region) and intralayer modes (in medium- and high-frequency regions). Moreover, layered compounds crystallizing either in rhombohedral, hexagonal or tetragonal space groups, show A (or B) and E modes. In rhombohedral $SnSb_2Te_4$, there are two pure interlayer modes ($E_g^1$ and $A_{1g}^1$), which have the lowest frequencies, and the other ten Raman- and IR-active modes are intralayer modes and have both medium and high frequency values (see Table 3 and Table S2). The two interlayer modes, also known as rigid layer modes, correspond to out-of-phase movements of the neighbor layers both along the $a-b$ plane ($E_g^1$ mode) and along the $c$-axis ($A_{1g}^1$ mode).

Figure S18 also shows the unpolarized HP-RS measurements up to 9 GPa. Pressure induces a monotonous shift of the Raman modes toward higher frequencies, except for two modes with negative slope near ambient pressure (see Figure 6). These two modes can be unambiguously assigned to
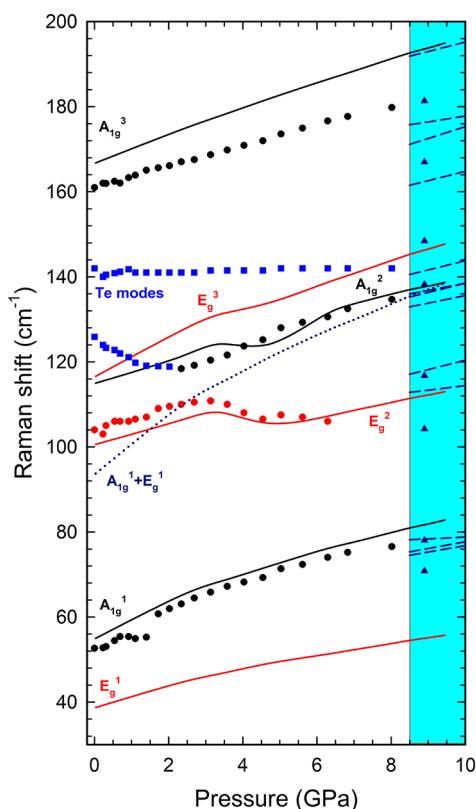
metallic Te,[100] and their appearance can be explained by the extreme sensitivity of some selenides and tellurides to visible laser radiation. In fact, Raman modes of trigonal Se and Te with negative slope have been recently identified in HP-RS studies of $As_2Te_3$[72] and $HgGa_2Se_4$.[101]

The pressure dependence of the experimental and theoretical Raman-active modes in $SnSb_2Te_4$ at HP (see Figure 6 and Table 3 and S1) shows a good agreement within a 5% accuracy interval. This feature is a clear sign of the good description reached by the *ab initio* simulations for this compound. For the sake of completeness, the evolution of the theoretical IR-active modes in $SnSb_2Te_4$ is also given in Figure S19 and S20.

Similar vibrational modes in the low- and high-frequency ranges of $SnSb_2Te_4$ are also observed in the parent binary compound $\alpha$-$Sb_2Te_3$ (see Figure S21 and Tables S1 and S2). However, there are four vibrational modes of $SnSb_2Te_4$ in the medium-frequency region (two Raman-active and two IR-active) that do not have correspondence on the $\alpha$-$Sb_2Te_3$ compound, because they are characteristic of the SL in ternary layered $BA_2X_4$ compounds. These extra modes in $SnSb_2Te_4$ arise from the vibrations involving the central Sn–Te2 bonds; in particular, out-of-phase vibrations of the Te2 atoms of the $SnTe_6$ polyhedral unit (see Figures S10 and S11).

It is well-known that the rocksalt-type structure of c-SnTe does not have any Raman-active mode but one IR-active mode with $T_{1u}$ symmetry that splits into a doubly degenerate transverse optical (TO) mode and a single longitudinal optical (LO) mode. It is interesting to note that the two extra Raman-active modes observed in $SnSb_2Te_4$ can be related to the two IR-active modes of c-SnTe (see Figure S22). In this context, it can be observed that phonons of similar nature in $SnSb_2Te_4$ and $\alpha$-$Sb_2Te_3$ are located around similar frequencies (Figure S21), so the position of the two medium-frequency modes in $SnSb_2Te_4$ is expected to be located at similar frequencies than in c-SnTe. In particular, there is a clear correlation between the $A_{1g}^2$ mode of $SnSb_2Te_4$ and the LO-type IR-active mode of c-SnTe at room pressure[102] (see Table S1) that is also extended at HP (see Figure S22). Therefore, our Raman results for $SnSb_2Te_4$ open a new way to characterize the lattice dynamics of binary compounds with forbidden Raman modes, like those crystallizing in the rocksalt-type structure as c-SnTe, by means of RS measurements in more complex compounds containing similar atomic coordination as those in the binary compounds. A similar example may be the case of rocksalt-type MgO, whose LO IR-active mode (738 cm$^{-1}$)[103] is consistent with the frequency of the highest Raman-active mode (715 cm$^{-1}$) in $MgTiO_3$ with s.g. $R\overline{3}$.[104]

An anomalous decrease of the experimental and theoretical frequency of Raman-active modes $A_{1g}^2$ and $E_g^2$ (see Figure 6) and of the theoretical frequency of IR-active modes $E_u^2$ and $A_u^2$ (see Figure S19) of $SnSb_2Te_4$ is observed above 3.0 GPa. The softening of these vibrational modes, mainly related to Sn–Te vibrations could be *a priori* ascribed to the pressure-induced IPT around 2 GPa, which is similar to that occurring in $\alpha$-$Sb_2Te_3$ between 2.5 and 3.5 GPa.[68,105,106] A close look at our theoretical simulations (see Figures S10 and S11) reveal that the $E_g^2$ and $E_u^2$ modes in $SnSb_2Te_4$ are mainly Sn–Te bending modes with a slight stretching contribution, while the $A_{1g}^2$ and $A_{2u}^2$ modes are mainly Sn–Te stretching modes. Since stretching modes mainly depend on the bonding force constant and the bonding distance, the softening of these vibrational modes involving Sn–Te2 bonds could likely be



**Figure 6.** Pressure dependence of the experimental (symbols) and theoretical (lines) Raman-active mode frequencies in $SnSb_2Te_4$. Dotted line represents the pressure dependence of the $A_{1g}^1 + E_g^1$ combination at Γ, while dashed lines represent the Raman-active modes expected for $\beta$-$Sb_2Te_3$.

related either to a strong decrease of the Sn−Te2 bonding force constant (depending on the charge density) or to a strong increase of the interatomic distance. However, neither an increase of the Sn−Te2 interatomic distance (Figure S3) nor a decrease of the Sn−Te2 bond charge density (Figure S26) have been observed in the whole studied pressure range. Another possibility to explain the softening is that there is a change of the character of the stretching modes so that they become more bending-like than stretching-like. To prove that, we have looked at the angle between the *ab*-plane and the Sn−Te2 bond (see Figure S5b). It can be observed that a subtle change in this angle occurs around 4 GPa, but the increase of the angle value suggests that these vibrational modes acquire an increasing stretching character, which is inconsistent with the loss of bonding strength.

After all these considerations, we have concluded that the softening of the medium-frequency phonons in $SnSb_2Te_4$ could only be explained by a Fermi resonance effect.[107] A Fermi resonance occurs when there is a strong anharmonic interaction of a first-order phonon with a two-phonon combination containing a high density of states. In such a case, a frequency shift and a change in the intensity and width of the first-order vibrational mode occurs. The Fermi resonance is a rare phenomenon in solids that has been observed in copper halides, molecules and defect modes.[108−111] In $SnSb_2Te_4$, the sum of the frequencies of the $A_g^1$ and $E_g^1$ at $\Gamma$ almost coincides in frequency with the $E_g^2$ mode at 2 GPa; i.e. the pressure range close to the onset of the softening of this mode in $SnSb_2Te_4$ (Figure 6). The anomalous softening of the Sn−Te related modes in $SnSb_2Te_4$ is also reproduced, even more clearly, by the theoretically predicted evolution of the IR-active LO-mode of c-SnTe at HP (see Figure S22). Note that the frequency of this mode in c-SnTe at 2 GPa coincides in frequency at $\Gamma$ with twice the value of the TO mode when a change in the slope occurs (Figure S22). Therefore, we conclude that c-SnTe likely exhibits a Fermi resonance in the IR-active LO mode that is also reproduced in the medium-frequency range of $SnSb_2Te_4$. This result gives further support to our previous interpretation of the relationship between the vibrational modes of $SnSb_2Te_4$ and c-SnTe. In summary, we attribute the softening of $A_g^2$ and $E_g^2$ of $SnSb_2Te_4$ at HP to a pressure-induced Fermi resonance caused by the coincidence of the frequencies of these first-order Raman modes and the combination of $A_g^1$ and $E_g^1$ modes along the whole BZ.

We want to comment that the existence of the Fermi resonance is not related to any kind of mechanical or dynamical instability of the crystalline structure. In fact, our theoretical phonon dispersion curves calculated at several pressures before and after the Fermi resonance (not shown) do not show any kind of instability; i.e. no soft phonons or phonons with imaginary frequencies. In this context, we must note that elastic constants of cooper halides show a normal increase with increasing pressure up to the first-order phase transition with no sign of mechanical instability.[112] On the other hand, it is well-known that the negative thermal expansion of cooper halides is related to the softening of acoustic modes at the Brillouin zone, as it occurs for many cubic compounds, but with no sign of dynamic instability (imaginary frequencies) have been shown even at the pressures of the first-order phase transition.[113] Therefore, we can conclude that the Fermi resonance in $SnSb_2Te_4$, and likely c-SnTe, is not related to any mechanical or dynamical instability.

To close this section, we have calculated the phonon dispersion curves in $SnSb_2Te_4$ at 0, 2, and 4 GPa (see Figure S23) in order to understand the nature of the IPT close to 2 GPa previously discussed. As observed, our calculations do not show softening of any of the phonon branches. This result suggests that the pressure-induced IPT found above 2 GPa, cannot be assigned to a higher order IPT and must be of higher-order.

In summary, our analysis of the lattice dynamics of $SnSb_2Te_4$ at HP shows the layered character of this compound and a good agreement between our experimental and theoretical data. The Raman-active modes of $SnSb_2Te_4$ have been explained in relation to its binary parents $\alpha$-$Sb_2Te_3$ and c-SnTe and it has been proved that modes that cannot be observed by Raman scattering in c-SnTe can be observed with this technique in $SnSb_2Te_4$ containing similar $SnTe_6$ polyhedra than c-SnTe. Additionally, the anomalous behavior of two Raman-active and two IR-active modes above 3.5 GPa in the medium-frequency region, which are characteristic of the SLs and related to Sn−Te vibrations, has been attributed to a Fermi resonance that also occurs in c-SnTe near 2 GPa. Finally, we have proved, with the help of the phonon dispersion curves for $SnSb_2Te_4$ at different pressures, that the IPT occurring in $SnSb_2Te_4$ close to 2 GPa is not of second-order but is of higher order, as expected for an IPT of electronic origin.

**4.3. Electrical Resistance Measurements under Pressure.** In the parent binary compound $\alpha$-$Sb_2Te_3$, the reported pressure-induced IPT was argued to be associated to a pressure-induced ETT around 3.5 GPa.[68] This result has motivated us to carry out resistance measurements and theoretical calculations of the electronic band structure at different pressures in order to verify if a pressure-induced ETT could also be observed in $SnSb_2Te_4$. This kind of measurements have been previously validated by other works[114] up to 50 GPa.

Two abrupt variations in the pressure dependence of the electrical resistance of $SnSb_2Te_4$ above 2 and 8 GPa have been observed (see Figure 7). The variation above 8 GPa can be
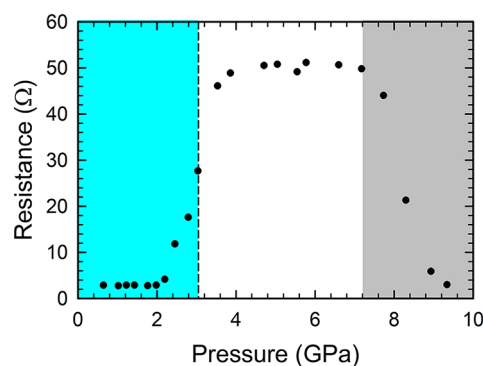
**Figure 7.** Evolution of the resistance of compressed $SnSb_2Te_4$ recorded during the upstroke.

ascribed to the PID of the sample, already commented in section A, which is similar to that observed also above 8 GPa in $SnBi_2Te_4$.[40] This result confirms our formation enthalpy analysis (Figure 5) that suggest that $SnBi_2Te_4$ likely undergoes also a PID. Furthermore, the low resistance measured above 8 GPa can be ascribed to the metallic nature of the HP phases of $\alpha$-$Sb_2Te_3$ and c-SnTe.[67,115]

Below 8 GPa, we can distinguish two different ranges in the evolution of the electrical resistance of $SnSb_2Te_4$ below and above 2 GPa. At the LPs, $SnSb_2Te_4$ evidence a very low electrical resistance (constant from room pressure to 2 GPa), whose behavior and values are typical of a degenerate semiconductor. Previous results on the literature[32] have shown that these results correspond to a lack of stoichiometric vacancies, which leads to the formation of a p-type degenerate semiconductor whose carriers are created by cation vacancies. Above 2 GPa, there is a drastic increase of the electrical resistance, which traditionally has been associated in the literature to the creation of structural defects along an ongoing phase transition.[116] These defects might create donor levels that modify the carrier concentration of the material. Recently, Reindl and co-workers have explored the change of disorder in this kind of materials observing the same effect we reproduce here and assumed it to be due to a metal−insulator transition.[117] In $SnSb_2Te_4$, the IPT occurring around 2 GPa might be the responsible for the creation of donor levels associated to defects. These could be able to trap p-carriers, thus helping to pass from a degenerate to a nondegenerate semiconductor or acting as scattering centers that decrease carrier mobility. In any case, the decrease in carrier mobility would be an indication of a decrease of the p-type character of the electrical conduction in $SnSb_2Te_4$, similar to that occurring in ZnTe between 7 and 11 GPa.[116] Thus, the decrease of the conductivity evidenced by $SnSb_2Te_4$ above 2 GPa could be exploited to overcome one of the main problems of TIs; i.e. the non-observation of surface carrier conductivity is due to its masking by bulk carrier conductivity.[118]

Regarding electronic band structure calculations, we obtain that $SnSb_2Te_4$ is an indirect bandgap semiconductor with a bandgap energy $E_g = 0.12$ eV at room pressure, similar to that previously obtained,[16] and that the bandgap energy decreases with increasing pressure leading to a closing of the bandgap above 4.5 GPa (see Figure S24). Since our GGA-PBEsol calculations are known to yield underestimated bandgaps when (semi)local functionals are employed, the value of the real bandgap is expected to be above 0.2 eV at room pressure[11] and the real metallization must occur at higher pressures. In fact, the predicted lack of metallization at LP and the negative slope of the bandgap are compatible with the above-mentioned explanation of the evolution of the electrical resistance at HP. However, we cannot neglect the fact that the lack of hydrostatic conditions above 2.5 GPa due to the use of a solid PTM may blur the interpretations of the changes observed in the electrical properties of the material.

Regarding the possibility of an ETT in $SnSb_2Te_4$, our electronic band structure calculations show that the valence band shows no major changes in the whole range of studied pressures; however, there are considerable changes in the conduction band. At 0 GPa, the conduction band minimum is around the Γ point, but there is a considerable downward shift of the local minimum of the conduction band at the F point with pressure. This minimum becomes the absolute minimum of the conduction band above 4.5 GPa. Therefore, a possible ETT could be expected for an n-type material between 0 and 4.5 GPa. Since we work with a p-type material, we cannot attribute the change in resistance near 2 GPa to an ETT.

In summary, our electrical measurements in $SnSb_2Te_4$ show a small resistance at LP, typical of a degenerate semiconductor, and an increase of the electrical resistance above 2.0 GPa, attributed to the generation of defects due to the pressure-induced IPT. Finally, the decrease of the electrical resistance above 8 GPa is attributed to the metallic nature of the HP phases of $\alpha$-$Sb_2Te_3$ and c-SnTe due to the decomposition of $SnSb_2Te_4$ above 7 GPa. The behavior of the electrical resistance in $SnSb_2Te_4$ is consistent with our calculations of the electronic band structure that do not show metallization up to 8 GPa when the value of the theoretical bandgap is corrected.

**4.4. Electronic Topology under Pressure.** Rhombohedral $SnSb_2Te_4$ contains different kind of bonds. The vdW interaction between Te1 atoms belonging to different SLs is widely accepted in the scientific community; however, recent studies in chalcogenides have established the difference in the interatomic distance with respect to their vdW radii as an indication that this Te1−Te1 bond is not purely vdW. Thus, the assignation to this separation as vdW gap would be reinterpreted as vdW-like gap.[37,119]

The nature of the bonds between Sn−Te2, Sb−Te2, and Sb−Te1 are also the focus of intense debates. According to the Lewis' octet rule, $Sb^{3+}$ and $Sn^{2+}$ cations bonded to $Te^{2−}$ atoms should not have the octahedral coordination observed here, and this has been explained in the literature by delocalization of the charge by means of a chalcogen or hypervalent interaction.[120,121] In our case, the bonds are not established among chalcogen atoms, but between a chalcogen anion and different types of cations. This scenario may imply that we can neglect the chalcogen bonding as responsible for the interactions above-mentioned. On the other hand, the concept of hypervalency has been extensively studied and is a subject of strong discussions up to date. The most recent and accepted quantitative approximation to this concept was performed by Durrant,[122] where the valence equivalent electron parameter defined by "the formal shared electron count at a given atom, obtained by any combination of valid and covalent resonant form". This parameter discerns between molecules that can be considered as hypervalent or obeying a "modified octet rule". For instance, $XeF_2$ molecule[123] should obey a modified octet rule, the same as occurs for our $SbTe_6$ and $SnTe_6$ polyhedral units. The bond character for the $XeF_2$ molecule has been explained by the concept of a charge-shift bond, which is usually established between a central atom with low ionization potential and a strongly electronegative ligand. In our case, the $SbTe_6$ or $SnTe_6$ polyhedral units show no significant difference between their electronegativities. The unfortunate attempt to describe the chemical interactions involved on these polyhedral units led us to explore new kind of bonds. In this context, the interactions in both parent binary compounds of $SnSb_2Te_4$ ($\alpha$-$Sb_2Te_3$ and c-SnTe) have been recently explained by the so-called metavalent bonding,[34−37] where electrons are shared between nearest neighbors without electron transfer allowing to exceed the octet rule limitation. The use of this denomination is still under controversy, because some authors claimed that the bonding in chalcogenides can be explained by molecular-orbital approach or valence-bond theory of hyper-bonding,[124] where that hypervalence bonding is a special case of charge-shift bonding.[125]

*4.4.1. Bader Charge Analysis.* In recent HP works of $\alpha$-$Sb_2Te_3$, the occurrence of a pressure-induced IPT was studied on the light of the electron density evolution under pressure.[75] Additionally, the pressure-induced ETT was interpreted on the light of the evolution of the Bader charges at HP.[105] Since the occurrence of a pressure-induced ETT depends on the location of the Fermi level, it is rather doubtful that the pressure at
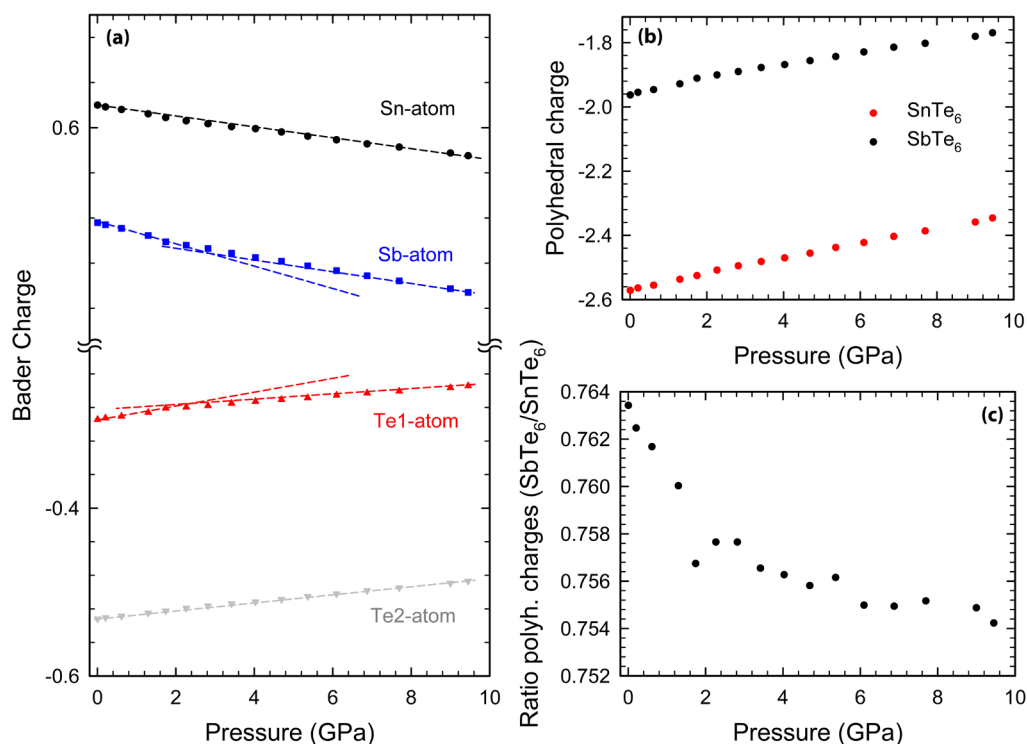
**Figure 8.** HP evolution of the (a) Bader charge of the different crystallographic atoms, (b) charge of the different polyhedral units, and (c) ratio between the polyhedral charges.
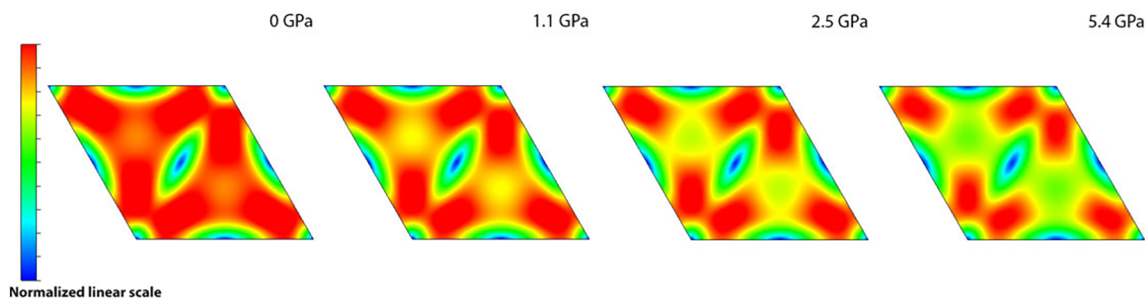


**Figure 9.** Evolution of the reduced density gradient (NCI) in the interlayer plane with increasing pressure. Blue color corresponds to zero interaction and red color corresponds to 1 (maximum interaction in the interlayer zone).

which an ETT is observed can be determined with the study of the theoretical Bader charge analysis, which is independent of the location of the Fermi level. However, a change in the evolution of the Bader charges at HP can be indicative of a pressure-induced IPT, not related with a variation of the Fermi level.

Figure 8a shows the pressure dependence of the Bader charges for each of the constituent atoms of $SnSb_2Te_4$. The Bader charges of the internal atoms of the SLs (Sn and Te2 atoms), related to the $SnTe_6$ polyhedral units, are larger than those of the external atoms of the SL (Sb and Te1) related to the $SbTe_6$ polyhedral units, and describe a monotonous trend with respect to pressure following an almost linear behavior with a small kink near 2 GPa. On the other hand, the pressure evolution of the Bader charges of the most external atoms of the SLs cannot be fitted to a single linear trend and two linear fits below and above 2 GPa are required.

The comparison between the polyhedral net charges contained in the two octahedral units that compose this ternary material (Figure 8b) reveals a clear change of trend

above 2 GPa (Figure 8c). An abrupt charge transfer from $SbTe_6$ toward $SnTe_6$ occurs up to 2 GPa and ceases above this pressure. This evolution can be explained as follows: At LP, the closing of the interlayer gap leads to a strong charge redistribution of the external $SbTe_6$ unit that lead to a charge transfer to the $SnTe_6$ unit. Above 2 GPa, the vdW-like space is already closed and no further charge is transferred between both $SnTe_6$ and $SbTe_6$ units so their Bader charges evolve similarly under pressure. In summary, the charge redistribution between the polyhedral units is consistent with Te1 atoms being involved in the $SbTe_6$ octahedral units and being the ones responsible for the vdW interactions in the interlayer gap that define the IPT around 2 GPa in $SnSb_2Te_4$.

*4.4.2. Non-covalent Interaction Analysis.* We have performed non-covalent interaction (NCI) simulations[64,65] to probe the evolution of the low electron density regions at the interlayer space between two neighboring SLs. Figure S25 highlight the vdW-like interactions at the interlayer (Te1−Te1) space at LP and their evolution toward more localized interactions at HP. A 2D data profile of the NCI of the

interlayer space between two SLs is represented in Figure 9. This figure can be interpreted as follows: At LP, the electron density cloud is very flat and delocalized but the fact that the interatomic distance is smaller than the vdW diameter might imply a certain localized character, even if the vdW bond is predominant. Above 2 GPa, bonds become more localized; thus, clear bonds appear among polyhedra of neighbor SLs. Overall, all results point at charge localization with increasing pressure so that the Te1−Te1 vdW nature of the interlayer space is no longer governing the response of the solid above 2 GPa.

*4.4.3. Electronic Density Analysis.* A more quantitative analysis of the electronic topology can be done by analyzing the evolution of two parameters, such as the electron charge density, $\rho(\vec{r})$, and its Laplacian, $\nabla^2 \rho(\vec{r})$, at the bond critical point (BCP), which can be defined by the point of minimum electron density between two bonded atoms (following the electron density gradient). This method allows us to determine the bonding character of the four bounds found in $SnSb_2Te_4$ (Te1−Te1, Sb−Te1, Sb−Te2, and Sn−Te2).

With regards to the Te1−Te1 interaction, we can distinguish its predominant vdW character at LPs, determined by a low $\rho(\vec{r})$ and a positive value of the $\nabla^2 \rho(\vec{r})$ at the BCP (see Figure S26). However, these values are higher than those found in vdW complexes.[126] Then, we cannot neglect that the interlayer interaction may be influenced by a certain charge transfer caused by the Sb−Te1 bond, as suggested by Cheng et al.[37] An increase of both parameters at HP is coherent with the decrease of vdW character[127] we have already observed and commented in the previous section. At LP, Te1 atoms are bonded to three Sb atoms and at close vicinity with other three Te1 atoms, belonging to the neighboring layer, at much larger distance. At HP, the strong decrease of the interlayer Te1−Te1 distance gives rise to a stronger interaction between the Te atoms belonging to different layers, thus leading to a 6-fold coordination of the Te1 atoms. This Te1−Te1 interaction supports the evidence of the formation of more ionic bonds between the neighboring Te atoms since ionic bonds are characterized by large and positive $\rho(\vec{r})$ and positive $\nabla^2 \rho(\vec{r})$ at the BCP (see Table 4).

**Table 4. Values of the Electronic Charge Density and Its Laplacian at the BCP as well as the ELF along Different Types of Bonding**

|  | ionic | covalent | metavalent | metallic | van der Waals |
|---|---|---|---|---|---|
| $\rho(\vec{r})$ | large | large | medium | small | small |
| $\nabla^2\rho(\vec{r})$ | positive | negative | small (positive or negative) | positive | positive (small) |
| ELF | large | large | medium | small | small |

With respect to the Sb−Te2 and Sn−Te2 bonds, they possess similar values of $\rho(\vec{r})$ and $\nabla^2 \rho(\vec{r})$ at the BCP in the whole pressure range studied. In fact, the value of $\rho(\vec{r})$ for both bonds is intermediate between that of Sb−Te1 bond and the weak vdW interaction between Te1 atoms along the whole of the studied pressure range. In this context, we have to recall that both parent binary compounds, $\alpha$-$Sb_2Te_3$ and c-SnTe, have been considered as incipient metals,[34−37] therefore these values of $\rho(\vec{r})$ and $\nabla^2 \rho(\vec{r})$ could be characteristic parameters of metavalent bonding with partially delocalized electrons.

Regarding the Sb−Te1 bond, it evidences a very high $\rho(\vec{r})$ when compared to the overall interactions and a positive, although close to zero, value of the $\nabla^2 \rho(\vec{r})$ at the BCP in the whole pressure range studied. The high $\rho(\vec{r})$ value is typical of covalent or ionic bonding; however, the $\nabla^2 \rho(\vec{r})$ value must be negative (positive) for a covalent (ionic) bonding. Therefore, the small positive $\nabla^2 \rho(\vec{r})$ value suggests a mixture between the covalent and metavalent bonding.

In order to deepen into the analysis of the character of these two bonds, we have plotted the electronic localization function (ELF) along the different atomic interaction distances of $SnSb_2Te_4$; namely, Te1−Te1, Sb−Te1, Sb−Te2, and Sn−Te2 (see Figure 10 and Figure S27). ELF describes the character of bond formation between the involved atoms. At LPs, the low ELF values (close to 0.2) close to the center of the Te1−Te1 distance, exhibit the typical values of vdW bonds at LPs; however, this ELF signal increases rapidly with pressure toward values characteristic of an ionic-type bond in good agreement with the results observed from the BCP electronic topological analysis. Therefore, our results support the main vdW nature of the Te1−Te interlayer bonds in $SnSb_2Te_4$ at room pressure.

In this context, it is important to note that the distance between the interatomic Te1−Te1 distance is smaller than the double of the Te vdWs radii. This means that Te1−Te1 interlayer bond in $SnSb_2Te_4$ has a stronger interaction than, for instance, Se−Se interlayer bond in layered InSe, GaSe and $NbSe_2$, which are considered to have a pure vdW interaction. The larger values of the spacing in vdW gaps in transition-metal dichalcogenides with respect to $A^V_2X^{VI}_3$ compounds and related materials is clearly shown in literature.[38] In fact, different types of polymorphs with different stacking sequences can be found with similar energies in layered compounds with pure vdW interactions, as InSe, GaSe, and most transition-metal dichalcogenides. The existence of polymorphs does not occur in $A^V_2X^{VI}_3$ compounds and its ternary derivatives, as already commented by Gaspard and Ceolin,[128] who already suggested that V−VI interlayer bonds could be considered as formed by weak covalent forces. However, recent calculations on $Ge_3Sb_2Te_6$ by Sa et al.[129] have shown that the Te−Te interlayer forces can be considered of vdW type because the strength of this interaction deviates a small quantity from a pure vdW interaction. Our results agree with results of Sa et al. since the low electronic density at the bond critical point of the Te1−Te1 interlayer interaction in $SnSb_2Te_4$ at 0 GPa (see in Figure S25) is typical of delocalized bonds. Consequently, the Te1−Te1 interlayer interaction in $SnSb_2Te_4$ at 0 GPa is closer to the vdW interaction than to other stronger interactions. We have also to note that interlayer interactions stronger than typical vdW bonds have been already found in layered chalcogenides BiTeX (X = Cl, Br, I) since these are polar semiconductors with Te−X interlayer bonds that show a mixture of vdW and polar character.[130]

Moreover, we have demonstrated in this manuscript that the strength of the Te1−Te1 interaction rises up with pressure. This strengthening of the vdW interlayer interaction with increasing pressure has been observed in a number of layered materials. Consequently, the vdW interlayer interaction is only present in chalcogenide layered materials at very low pressures and they cannot be considered any more of vdW type at HP; i.e., above 2 GPa in $SnSb_2Te_4$.

In the case of the Sb−Te1 bond, the ELF value close to the center of its respective interatomic distance is high enough (0.7) to ensure we are dealing with a strong bond, coherent
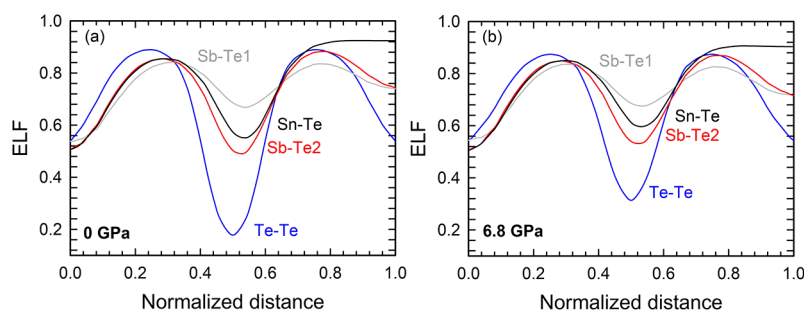
**Figure 10.** Pressure dependence of the ELF along the path of the Sb−Te1, Sb−Te2, Sn−Te, and Te−Te bonds at 0 GPa (a) and 6.8 GPa (b).

with the polar-covalent results previously obtained from the BCP analysis. Regarding the ELF signals between the Sn−Te and the Sb−Te2 bonds, these have a medium value (0.5−0.6), which is close to the center of the interatomic distance. This value has been associated in the literature to be of metavalent bonding character.[34,35,131,132] The intermediate values of $\rho(\vec{r})$ of both bonds, at the BCP and ELF, can be explained by the partial delocalization of electrons of this type of bonding, which stems from the sharing of electrons between several bonds; i.e. there is one single electron per bond instead of two in a typical covalent bond. Therefore, our ELF values support the previous analysis of $\rho(\vec{r})$ and $\nabla^2 \rho(\vec{r})$ at the BCP for both interactions. In this way, we have established a new form of identifying metavalent bonds; i.e. they are characterized by an intermediate value of $\rho(\vec{r})$ and a low positive value of $\nabla^2 \rho(\vec{r})$. The classification of the different bondings according to $\rho(\vec{r})$, $\nabla^2 \rho(\vec{r})$ and ELF are summarized in Table 4.

In summary, we conclude that the changes observed both at the Bader and NCI analyses reflect the IPT occurring from the rhombohedral $SnSb_2Te_4$ close to 2 GPa. This IPT is strongly related to the hardening of the Te1−Te1 interlayer interaction and the loss of their predominant vdW character. Moreover, we have shown that Sb−Te1 bonds are polar covalent bonds, whereas the Sb−Te2 and the Sn−Te2 bonds may fall into what has been recently defined to be the metavalent-type bonding. Finally, we have fully characterized all the bond types present in $SnSb_2Te_4$ by analyzing the electron density. Thus, we have proposed a new method (by using the concepts of $\rho(\vec{r})$ and $\nabla^2 \rho(\vec{r})$ at the BCP) to identify the bond character in complex structures, where a coexistence of several types of interactions occurs.

## 5. CONCLUSION

Our study of the compressed rhombohedral phase of $SnSb_2Te_4$ at room temperature shows that the rhombohedral phase is stable up to 7 GPa and that a decomposition of the sample occurs above this pressure. This behavior has been framed within the orbital radii map of the tellurium-based ternary chalcogenides (that has been extended) and a possible path at HP has been described for $SnSb_2Te_4$ that can be useful to understand other isostructural compounds of the $BA_2Te_4$ family.

The compressed rhombohedral structure of $SnSb_2Te_4$ shows an isostructural phase transition above 2 GPa that is mainly caused by a change in the compressibility of the interlayer space, governed mostly by vdW interactions between the external Te atoms of the SLs, which also dominate the behavior of the unit-cell volume under compression. The change in the compressibility of the interlayer space is clearly

reflected on the analysis of the pressure dependence of the calculated electron density topology.

The study of the lattice dynamics of $SnSb_2Te_4$ under compression has allowed us to understand the atomic vibrations of the different phonons and assign the mode symmetries of the Raman-active modes. Furthermore, the description of the atomic vibrations has been compared with their parent binary compounds (c-SnTe and $\alpha$-$Sb_2Te_3$). A softening of vibrational modes mainly related to the Sn−Te bonds occurs above 3 GPa, and such a feature has been explained within the framework of the Fermi resonance. Our calculations predict that the Fermi resonance must also be observed in the HP dependence of IR-active modes of parent binary c-SnTe around 2 GPa. Our results show strong correlation between the vibrational modes of $SnSb_2Te_4$ and those of its parent binary compounds. In fact, the Raman spectrum of $SnSb_2Te_4$ shows vibrational modes that are forbidden in c-SnTe; thus, showing a novel way to experimentally observe the forbidden vibrational modes of some compounds.

We have also undertaken a study of the pressure dependence of the electrical properties of $SnSb_2Te_4$ with unintentionally p-type semiconducting character in order to verify if an ETT could be observed. The change in the electrical resistance above 8 GPa has been attributed to the sample decomposition; however, a drastic increase in resistance was observed above 2 GPa. This increase has not been attributed to an ETT due to the p-type character of our sample, but to the generation of defects on the ongoing IPT passing from a p-type degenerate to a nondegenerate semiconductor by the reduction of the hole carrier concentration. This result allows the tuning of the electrical properties to improve the TI capabilities of this compound.

Finally, our electron density topology analysis shows that the IPT around 2 GPa is related to the loss of the predominant vdW character by an increment of the ionic character of the interaction between the Te1 atoms of neighbor SLs, so the hardening of the Te1−Te1 bond may be the cause of the IPT. The lack of soft phonon branches along the Brillouin zone confirms that the observed IPT is related to a phase transition of higher order than 2; i.e. it is an IPT of electronic origin.

The analysis of the ELF of the Sb−Te1 interaction displays a polar covalent bond character, which remains unalterable under compression. However, the most interesting analysis is obtained when studying the ELF along the Sb−Te2 and Sn−Te interactions, which show the typical intermediate values expected for metavalent bonding. The evaluation of their electronic densities and respective Laplacians at the BCP provides a new criterion to identify these interactions when the material is very complex and different kinds of bonds coexist.

In summary, our study provides new insights into the physics and chemistry of ternary topological insulators of the tetradymite-like ternary $BA_2X_4$ materials and highlights the importance of the study of the evolution of the chemical bonds under pressure of topological insulators in order to understand the origin of isostructural phase transitions observed in this family of compounds and the possibility to tune their exceptional properties in a better way than in binary topological insulators.

## ASSOCIATED CONTENT

### Supporting Information

The Supporting Information is available free of charge at https://pubs.acs.org/doi/10.1021/acs.inorgchem.0c01086.

Additional graphs and explanations about the structural features of compressed $SnSb_2Te_4$, description of the different vibrational modes found in $SnSb_2Te_4$ together with the theoretical evolution of the frequency of the Raman-active and IR-active modes under pressure and the dispersion curve at several pressures, and finally, a more detailed description of the pressure dependence of the topological electronic properties of $SnSb_2Te_4$ (PDF)

## AUTHOR INFORMATION

### Corresponding Author

Juan A. Sans − *Instituto de Diseño para la Fabricación y Producción Automatizada, MALTA-Consolider Team, Universitat Politècnica de València, Valencia, Spain;* orcid.org/0000-0001-9047-3992; Email: juasant2@upv.es

### Authors

Rosario Vilaplana − *Centro de Tecnologías Físicas, MALTA-Consolider Team, Universitat Politècnica de València, Valencia, Spain;* orcid.org/0000-0003-0504-2157

E. Lora da Silva − *Instituto de Diseño para la Fabricación y Producción Automatizada, MALTA-Consolider Team, Universitat Politècnica de València, Valencia, Spain;* orcid.org/0000-0002-7093-3266

Catalin Popescu − *ALBA-CELLS, Barcelona, Spain*

Vanesa P. Cuenca-Gotor − *Instituto de Diseño para la Fabricación y Producción Automatizada, MALTA-Consolider Team, Universitat Politècnica de València, Valencia, Spain;* orcid.org/0000-0003-0819-8528

Adrián Andrada-Chacón − *Departamento de Química-Física, MALTA-Consolider Team, Universidad Complutense de Madrid, Madrid, Spain*

Javier Sánchez-Benitez − *Departamento de Química-Física, MALTA-Consolider Team, Universidad Complutense de Madrid, Madrid, Spain;* orcid.org/0000-0002-3108-6594

Oscar Gomis − *Centro de Tecnologías Físicas, MALTA-Consolider Team, Universitat Politècnica de València, Valencia, Spain;* orcid.org/0000-0001-6763-0638

André L. J. Pereira − *Instituto de Diseño para la Fabricación y Producción Automatizada, MALTA-Consolider Team, Universitat Politècnica de València, Valencia, Spain; Grupo de Pesquisa de Materiais Fotonicos e Energia Renovavel - MaFER, Universidade Federal da Grande Dourados, Dourados, MS 79825-070, Brazil;* orcid.org/0000-0003-4757-8080

Plácida Rodríguez-Hernández − *Departamento de Física, MALTA-Consolider Team, Instituto de Materiales y Nanotecnología, Universidad de La Laguna, Tenerife, Spain;* orcid.org/0000-0002-4148-6516

Alfonso Muñoz − *Departamento de Física, MALTA-Consolider Team, Instituto de Materiales y Nanotecnología, Universidad de La Laguna, Tenerife, Spain;* orcid.org/0000-0003-3347-6518

Dominik Daisenberger − *Diamond Light Source Limited, Didcot, Oxon, England*

Braulio García-Domene − *Departamento de Física Aplicada-ICMUV, MALTA-Consolider Team, Universidad de Valencia, Valencia, Spain*

Alfredo Segura − *Departamento de Física Aplicada-ICMUV, MALTA-Consolider Team, Universidad de Valencia, Valencia, Spain;* orcid.org/0000-0002-9979-1302

Daniel Errandonea − *Departamento de Física Aplicada-ICMUV, MALTA-Consolider Team, Universidad de Valencia, Valencia, Spain;* orcid.org/0000-0003-0189-4221

Ravhi S. Kumar − *Department of Physics, University of Illinois at Chicago, Chicago, Illinois 60607-7059, United States*

Oliver Oeckler − *Institut für Mineralogie, Kristallographie und Materialwissenschaft, Universität Leipzig, Leipzig, Germany;* orcid.org/0000-0003-0149-7066

Philipp Urban − *Institut für Mineralogie, Kristallographie und Materialwissenschaft, Universität Leipzig, Leipzig, Germany*

Julia Contreras-García − *CNRS, UMR 7616, Laboratoire de Chimie Théorique, F-75005 Paris, France*

Francisco J. Manjón − *Instituto de Diseño para la Fabricación y Producción Automatizada, MALTA-Consolider Team, Universitat Politècnica de València, Valencia, Spain;* orcid.org/0000-0002-3926-1705

Complete contact information is available at:
https://pubs.acs.org/10.1021/acs.inorgchem.0c01086

### Author Contributions

The manuscript was written through contributions of all authors. All authors have given approval to the final version of the manuscript.

### Notes

The authors declare no competing financial interest.

## REFERENCES

(1) Mellnik, A. R.; Lee, J. S.; Richardella, A.; Grab, J. L.; Mintun, P. J.; Fischer, M. H.; Vaezi, A.; Manchon, A.; Kim, E.-A.; Samarth, N.; Ralph, D. C. Spin-transfer torque generated by a topological insulator. *Nature* **2014**, *511*, 449−451.

(2) Chen, Y. L.; Analytis, J. G.; Chu, J.-H.; Liu, Z. K.; Mo, S.-K.; Qi, X. L.; Zhang, H. J.; Lu, D. H.; Dai, X.; Fang, Z.; Zhang, S. C.; Fisher, I. R.; Hussain, Z.; Shen, Z.-X. Experimental Realization of a Three-Dimensional Topological Insulator. *Science* **2009**, *325*, 178−181.

(3) Hsieh, D.; Xia, Y.; Qian, D.; Wray, L.; Dil, J. H.; Meier, F.; Osterwalder, J.; Patthey, L.; Checkelsky, J. G.; Ong, N. P.; Fedorov, A. V.; Lin, H.; Bansil, A.; Grauer, D.; Hor, Y. S.; Cava, R. J.; Hasan, M. Z. A tunable topological insulator in the spin helical Dirac transport regime. *Nature* **2009**, *460*, 1101−1105.

(4) Zhang, T.; Jiang, Y.; Song, Z.; Huang, H.; He, Y.; Fang, Z.; Weng, H.; Fang, C. Catalogue of topological electronic materials. *Nature* **2019**, *566*, 475−479.

(5) Vergniory, M. G.; Elcoro, L.; Felser, C.; Regnault, N.; Bernevig, B. A.; Wang, Z. A complete catalogue of high-quality topological materials. *Nature* **2019**, *566*, 480−485.

(6) Tang, F.; Po, H. C.; Vishwanath, A.; Wan, X. Comprehensive search for topological materials using symmetry indicators. *Nature* **2019**, *566*, 486−489.

(7) Zunger, A. Beware plausible predictions of fantasy materials. *Nature* **2019**, *566*, 447−449.

(8) Zhang, H.; Liu, C. X.; Qi, X. L.; Dai, X.; Fang, Z.; Zhang, S.-C. Topological insulators in Bi2Se3, Bi2Te3 and Sb2Te3 with a single Dirac cone on the surface. *Nat. Phys.* **2009**, *5*, 438−442.

(9) Xia, Y.; Qian, D.; Hsieh, D.; Wray, L.; Pal, A.; Lin, H.; Bansil, A.; Grauer, D.; Hor, Y. S.; Cava, R. J.; Hasan, M. Z. Observation of a large-gap topological-insulator class with a single Dirac cone on the surface. *Nat. Phys.* **2009**, *5*, 398−402.

(10) Taherinejad, M.; Garrity, K. F.; Vanderbilt, D. Wannier center sheets in topological insulators. *Phys. Rev. B: Condens. Matter Mater. Phys.* **2014**, *89*, 115102.

(11) Niesner, D.; Otto, S.; Hermann, V.; Fauster, Th.; Menshchikova, T. V.; Eremeev, S. V.; Aliev, Z. S.; Amiraslanov, I. R.; Babanly, M. B.; Echenique, P. M.; Chulkov, E. V. Bulk and surface electron dynamics in a p-type topological insulator SnSb$_2$Te$_4$. *Phys. Rev. B: Condens. Matter Mater. Phys.* **2014**, *89*, No. 081404.

(12) Rowe, D. M. *CRC Handbook of Thermoelectrics*; CRC Press Inc.: New York, 1995.

(13) Venkatasubramanian, R.; Siivola, E.; Colpitts, T.; O'Quinn, B. Thin-film thermoelectric devices with high room-temperature figures of merit. *Nature* **2001**, *413*, 597−602.

(14) Eremeev, S. V.; Koroteev, Y. M.; Chulkov, E. V. Effect of the atomic composition of the surface on the electron surface states in topological insulators A$_2^V$B$_3^{VI}$. *JETP Lett.* **2010**, *91*, 387.

(15) Menshchikova, T. V.; Eremeev, S. V.; Chulkov, E. V. On the origin of two-dimensional electron gas states at the surface of topological insulators. *JETP Lett.* **2011**, *94*, 106.

(16) Menshchikova, T. V.; Eremeev, S. V.; Chulkov, E. V. Electronic structure of SnSb$_2$Te$_4$ and PbSb$_2$Te$_4$ topological insulators. *Appl. Surf. Sci.* **2013**, *267*, 1−3.

(17) Concas, G.; de Pascale, T. M.; Garbato, L.; Ledda, F.; Meloni, F.; Rucci, A.; Serra, M. Electronic and structural properties of the layered SnSb$_2$Te$_4$ semiconductor: Ab initio total-energy and Mössbauer spectroscopy study. *J. Phys. Chem. Solids* **1992**, *53*, 791.

(18) Eremeev, S. V.; Menshchikova, T. V.; Silkin, I. V.; Vergniory, M. G.; Echenique, P. M.; Chulkov, E. V. Sublattice effect on topological surface states in complex (SnTe)$_{n>1}$(Bi$_2$Te$_3$)$_{m=1}$ compounds. *Phys. Rev. B: Condens. Matter Mater. Phys.* **2015**, *91*, 245145.

(19) Agaev, K. A.; Talybov, A. G. Electron-diffraction analysis of the structure of GeSb$_2$Te$_4$. *Kristallografiya* **1966**, *11*, 454−456.

(20) Imamov, R. M.; Semiletov, S. A.; Pinsker, Z. G. The crystal chemistry of semiconductors with octahedral and with mixed atomic coordination. *Soviet Phys. Cryst.* **1970**, *15*, 239.

(21) Kuznetsov, A. Y.; Pereira, A. S.; Shiryaev, A. A.; Haines, J.; Dubrovinsky, L.; Dmitriev, V.; Pattison, P.; Guignot, N. Pressure-Induced Chemical Decomposition and Structural Changes of Boric Acid. *J. Phys. Chem. B* **2006**, *110*, 13858−13865.

(22) Shelimova, L. E.; Karpinskii, O. G.; Konstantinov, P. P.; Avilov, E. S.; Kretova, M. A.; Zemskov, V. S. Crystal structures and

thermoelectric properties of layered compounds in the ATe-Bi$_2$Te$_3$ (A = Ge, Sn, Pb) systems. *Inorg. Mater.* **2004**, *40*, 451.

(23) Kuropatwa, B. A.; Assoud, A.; Kleinke, H. Effects of Cation Site Substitutions on the Thermoelectric Performance of Layered SnBi$_2$Te$_4$ utilizing the Triel Elements Ga, In, and Tl. *Z. Anorg. Allg. Chem.* **2013**, *639*, 2411−2420.

(24) Kuropatwa, B. A.; Kleinke, H. Thermoelectric Properties of Stoichiometric Compounds in the (SnTe)$_x$(Bi$_2$Te$_3$)$_y$ System. *Z. Anorg. Allg. Chem.* **2012**, *638*, 2640−2647.

(25) Banik, A.; Biswas, K. Synthetic of Natural van der Waals Heterostructures. *Angew. Chem., Int. Ed.* **2017**, *56*, 14561−14566.

(26) Shelimova, L. E.; Karpinskii, O. G.; Svechnikova, T. E.; Nikhezina, I. Y.; Avilov, E. S.; Kretova, M. A.; Zemskov, V. S. Effect of cadmium, silver, and tellurium doping on the properties of single crystals of the layered compounds PbBi$_4$Te$_7$ and PbSb$_2$Te$_4$. *Inorg. Mater.* **2008**, *44*, 371.

(27) Shu, H. W.; Jaulmes, S.; Flahaut, J. Système AsGeTe: III. Étude cristallographique d'une famille de composés a modèles structuraux communs: $\beta$-As$_2$Te$_3$, As$_4$GeTe$_7$ et As$_2$Ge$_n$Te$_{3+n}$ (n = 1 à 5). *J. Solid State Chem.* **1988**, *74*, 277−286.

(28) Zhukova, T. B.; Zaslavskii, A. I. Crystal-Structures of Compounds PbBi$_4$Te, PbBi$_2$Te$_4$, SnBi$_4$Te$_7$, SnBi$_2$Te$_4$, SnSb$_2$Te$_4$, and GeBi$_4$Te$_7$. *Sov. Phys. Crystallogr.* **1972**, *16*, 796.

(29) Adouby, K.; Abba Toure, A.; Kra, G.; Olivier-Fourcade, J.; Jumas, J. C.; Perez Vicente, C. Phase diagram and local environment of Sn and Te: SnTe-Bi and SnTe-Bi$_2$Te$_3$ systems. *C. R. Acad. Sci., Ser. IIc: Chim.* **2000**, *3*, 51.

(30) Zhukova, T. B.; Zaslavskii, A. I. Crystal Structures of PbBi$_4$Te$_7$, PbBi$_2$Te$_4$, SnBi$_4$Te$_7$, SnBi$_2$Te$_4$, SnSb$_2$Te$_4$, and GeBi$_4$Te$_7$. *Kristallografiya* **1971**, *16*, 918.

(31) Oeckler, O.; Schneider, M. N.; Fahrnbauer, F.; Vaughan, G. Atom distribution in SnSb$_2$Te$_4$ by resonant X-ray diffraction. *Solid State Sci.* **2011**, *13*, 1157−1161.

(32) Schafer, T.; Konze, P. M.; Huyeng, J. D.; Deringer, V. L.; Lesieur, T.; Muller, P.; Morgenstern, M.; Dronskowski, R.; Wuttig, M. Chemical Tuning of Carrier Type and Concentration in a Homologous Series of Crystalline Chalcogenides. *Chem. Mater.* **2017**, *29*, 6749−6757.

(33) Gallus, J. Lattice Dynamics in the SnSb2Te4 Phase Change Material. *Diplomarbeit*; Rheinisch-Westfälischen Technischen Hochschule Aachen: 2011.

(34) Wuttig, M.; Deringer, V. L.; Gonze, X.; Bichara, C.; Raty, J. Y. A Incipient Metals: Functional Materials with a Unique Bonding Mechanism. *Adv. Mater.* **2018**, *30*, 1803777.

(35) Raty, J. Y.; Schumacher, M.; Golub, P.; Deringer, V. L.; Gatti, C.; Wuttig, M. A Quantum-Mechanical Map for Bonding and Properties in Solids. *Adv. Mater.* **2019**, *31*, 1806280.

(36) Yu, Y.; Cagnoni, M.; Cojocaru-Mirédin, O.; Wuttig, M. Chalcogenide Thermoelectrics Empowered by an Unconventional Bonding Mechanism. *Adv. Funct. Mater.* **2020**, *30*, 1904862.

(37) Cheng, Y.; Cojocaru-Mirédin, O.; Keutgen, J.; Yu, Y.; KüPers, M.; Schumacher, M.; Golub, P.; Raty, J.-Y.; Dronskowski, R.; Wuttig, M. Understanding the Structure and Properties of Sesqui-Chalcogenides (i.e., V$_2$VI$_3$ or Pn$_2$Ch$_3$ (Pn = Pnictogen, Ch = Chalcogen) Compounds) from a Bonding Perspective. *Adv. Mater.* **2019**, *31*, 1904316.

(38) Kooi, B. J.; Wuttig, M. Chalcogenides by Design: Functionality through Metavalent Bonding and Confinement. *Adv. Mater.* **2020**, *32*, 1908302.

(39) Hsieh, W.-P.; Zalden, P.; Wuttig, M.; Lindenberg, A. M.; Mao, W. L. High pressure Raman spectroscopy of phase change materials. *Appl. Phys. Lett.* **2013**, *103*, 191908.

(40) Vilaplana, R.; Sans, J. A.; Manjón, F. J.; Sánchez-Benítez, J.; Popescu, C.; Gomis, O.; Pereira, A. L. J.; García-Domene, B.; Rodríguez-Hernández, P.; Muñoz, A.; Daisenberger, D.; Oeckler, O.; et al. Structural and electrical study of the topological insulator SnBi$_2$Te$_4$ at high pressure. *J. Alloys Compd.* **2016**, *685*, 962−970.

(41) Song, P.; Matsumoto, R.; Hou, Z.; Adachi, S.; Hara, H.; Saito, Y.; Castro, P. B.; Takeya, H.; Takano, Y. Pressure-induced

superconductivity in SnSb$_2$Te$_4$. *J. Phys.: Condens. Matter* **2020**, *32*, 235901.

(42) Fauth, F.; Peral, I.; Popescu, C.; Knapp, M. The New Material Science Powder Diffraction Beamline at ALBA Synchrotron. *Powder Diffr.* **2013**, *28*, S360−S370.

(43) Dewaele, A.; Loubeyre, P.; Mezouar, M. Equations of State of Six Metals above 94 GPa. *Phys. Rev. B: Condens. Matter Mater. Phys.* **2004**, *70*, 094112.

(44) Hammersley, A. P.; Svensson, S. O.; Hanfland, M.; Fitch, A. N.; Häusermann, D. Two-dimmensional detector software: From real detector to idealized image or two-theta scan. *High Pressure Res.* **1996**, *14*, 235−248.

(45) Toby, B. H. EXPGUI, A Graphical User Interface for GSAS. *J. Appl. Crystallogr.* **2001**, *34*, 210−213.

(46) Larson, A. C.; Von Dreele, R. B.General Structure Analysis System (GSAS). *Los Alamos National Laboratory Report LAUR 86-748*; 1994.

(47) Klotz, S.; Chervin, J.-C.; Munsch, P.; Le Marchand, G. Hydrostatic limits of 11 pressure transmitting media. *J. Phys. D: Appl. Phys.* **2009**, *42*, 075413.

(48) Errandonea, D.; Muñoz, A.; González-Platas, J. Comment on "High-pressure x-ray diffraction study of YBO$_3$/Eu$^{3+}$, GdBO$_3$, and EuBO$_3$: Pressure-induced amorphization in GdBO$_3$. *J. Appl. Phys.* **2014**, *115*, 216101.

(49) Mao, H. K.; Xu, J.; Bell, P. M. Calibration of the Ruby Pressure Gauge to 800 kbar under Quasi-Hydrostatic Conditions. *J. Geophys. Res.* **1986**, *91*, 4673−4676.

(50) Syassen, K. Ruby Under Pressure. *High Pressure Res.* **2008**, *28*, 75−126.

(51) Debernardi, A.; Ulrich, C.; Cardona, M.; Syassen, K. Pressure Dependence of Raman Linewidth in Semiconductors. *Phys. Status Solidi B* **2001**, *223*, 213−223.

(52) García-Domene, B.; Ortiz, H. M.; Gomis, O.; Sans, J. A.; Manjõn, F. J.; Munoz, A.; Rodríguez-Hernández, P.; Achary, S. N.; Errandonea, D.; Martínez-García, D.; Romero, A. H.; Singhal, A.; Tyagi, A. K. High Pressure Lattice Dynamical Study of Bulk and Nanocrystalline In$_2$O$_3$. *J. Appl. Phys.* **2012**, *112*, 123511.

(53) Hohenberg, P.; Kohn, W. Inhomogeneous Electron Gas. *Phys. Rev.* **1964**, *136*, B864.

(54) Blöchl, P. E. Projector Augmented-Wave Method. *Phys. Rev. B: Condens. Matter Mater. Phys.* **1994**, *50*, 17953.

(55) Kresse, G.; Hafner, J. Ab Initio Molecular Dynamics for Liquid Metals. *Phys. Rev. B: Condens. Matter Mater. Phys.* **1993**, *47*, 558.

(56) Perdew, J. P.; Ruzsinszky, A.; Csonka, G. I.; Vydrov, O. A.; Scuseria, G. E.; Constantin, L. A.; Zhou, X.; Burke, K. Restoring the Density-Gradient Expansion for Exchange in Solids and Surfaces. *Phys. Rev. Lett.* **2008**, *100*, 136406.

(57) Mujica, A.; Rubio, A.; Muñoz, A.; Needs, R. J. High pressure phases of group-IV, III−V, and II−VI compounds. *Rev. Mod. Phys.* **2003**, *75*, 863−912.

(58) Parlinski, K. see: http://www.computingformaterials.com/index.html. March 2020.

(59) Tang, W.; Sanville, E.; Henkelman, G. A grid-based Bader analysis algorithm without lattice bias. *J. Phys.: Condens. Matter* **2009**, *21*, 084204.

(60) Sanville, E.; Kenny, S. D.; Smith, R.; Henkelman, G. An improved grid-based algorithm for Bader charge allocation. *J. Comput. Chem.* **2007**, *28*, 899−908.

(61) Henkelman, G.; Arnaldsson, A.; Jónsson, H. A fast and robust algorithm for Bader decomposition of charge density. *Comput. Mater. Sci.* **2006**, *36*, 354−360.

(62) Yu, M.; Trinkle, D. R. Accurate and efficient algorithm for Bader charge integration. *J. Chem. Phys.* **2011**, *134*, 064111.

(63) http://theory.cm.utexas.edu/henkelman/code/bader/. March 2019.

(64) Johnson, E. R.; Keinan, S.; Mori-Sanchez, P.; Contreras-Garcia, J.; Cohen, A. J.; Yang, W. Revealing Noncovalent Interactions. *J. Am. Chem. Soc.* **2010**, *132*, 6498−6506.

(65) Contreras-Garcia, J.; Johnson, E. R.; Keinan, S.; Chaudret, R.; Piquemal, J.-P.; Beratan, D. N.; Yang, W. NCIPLOT: A Program for Plotting Noncovalent Interaction Regions. *J. Chem. Theory Comput.* **2011**, *7*, 625−632.

(66) Angel, R. J.; Gonzalez-Platas, J.; Alvaro, M. EosFit-7c and a Fortran module (library) for equation of state calculations. *Z. Kristallogr. - Cryst. Mater.* **2014**, *229*, 405−419.

(67) Zhou, D.; Li, Q.; Ma, Y.; Cui, Q.; Chen, C. Unraveling Convoluted Structural Transitions in SnTe at High Pressure. *J. Phys. Chem. C* **2013**, *117*, 5352−5357.

(68) Gomis, O.; Vilaplana, R.; Manjón, F. J.; Rodríguez-Hernández, P.; Pérez-González, E.; Muñoz, A.; Kucek, V.; Drasar, C. Lattice dynamics of Sb$_2$Te$_3$ at high pressures. *Phys. Rev. B: Condens. Matter Mater. Phys.* **2011**, *84*, 174305.

(69) Sakai, N.; Kajiwara, T.; Takemura, K.; Minomura, S.; Fujii, Y. Pressure-Induced Phase Transition in Sb$_2$Te$_3$. *Solid State Commun.* **1981**, *40*, 1045−1047.

(70) Wang, B.-T.; Souvatzis, P.; Eriksson, O.; Zhang, P. Lattice dynamics and chemical bonding in Sb$_2$Te$_3$ from first-principles calculations. *J. Chem. Phys.* **2015**, *142*, 174702.

(71) Pereira, A. L. J.; Sans, J. A.; Vilaplana, R.; Gomis, O.; Manjon, F. J.; Rodríguez-Hernandez, P.; Muñoz, A.; Popescu, C.; Beltran, A. Isostructural Second-Order Phase Transition of $\beta$-Bi$_2$O$_3$ at High Pressures: An Experimental and Theoretical Study. *J. Phys. Chem. C* **2014**, *118*, 23189−23201.

(72) Cuenca-Gotor, V. P.; Sans, J. A.; Ibáñez, J.; Popescu, C.; Gomis, O.; Vilaplana, R.; Manjón, F. J.; Leonardo, A.; Sagasta, E.; Suárez-Alcubilla, A.; Gurtubay, I. G.; Mollar, M.; Bergara, A. Structural, vibrational, and electronic study of $\alpha$-As$_2$Te$_3$ under compression. *J. Phys. Chem. C* **2016**, *120*, 19340−19352.

(73) Robinson, K.; Gibbs, G. V.; Ribbe, P. H. Quadratic Elongation: A Quantitative Measure of Distortion in Coordination Polyhedra. *Science* **1971**, *172*, 567−570.

(74) Baur, W. H. The geometry of polyhedral distortions. Predictive relationships for the phosphate group. *Acta Crystallogr., Sect. B: Struct. Crystallogr. Cryst. Chem.* **1974**, *30*, 1195.

(75) Walsh, A.; Watson, W. Influence of the Anion on Lone Pair Formation in Sn(II) Monochalcogenides: A DFT Study. *J. Phys. Chem. B* **2005**, *109*, 18868−18875.

(76) Skowron, A.; Boswell, F. W.; Corbett, J. M.; Taylor, N. J. Structure Determination of PbSb$_2$Se$_4$. *J. Solid State Chem.* **1994**, *112*, 251−254.

(77) Smith, P. K.; Parise, J. B. Structure Determination of SnSb$_2$S$_4$ and SnSb$_2$Se$_4$ by High-Resolution Electron Microscopy. *Acta Crystallogr., Sect. B: Struct. Sci.* **1985**, *B41*, 84−87.

(78) Iitaka, Y.; Nowacki, W. A Redetermination of the Crystal Structure of Galenobismutite, PbBi$_2$S$_4$. *Acta Crystallogr.* **1962**, *15*, 691.

(79) Gaspard, J.-P.; Ceolin, R. Hume-Rothery rule in V-VI compounds. *Solid State Commun.* **1992**, *84*, 839−842.

(80) Gaspard, J.-P.; Pellegatti, A.; Marinelli, F.; Bichara, C. Peierls instabilities in covalent structures I. Electronic structure, cohesion and the Z = 8 − N rule. *Philos. Mag. B* **1998**, *77*, 727−744.

(81) Seo, D.-K.; Hoffmann, R. What Determines the Structures of the Group 15 Elements? *J. Solid State Chem.* **1999**, *147*, 26−37.

(82) Zhang, H.; Liu, C.-X.; Zhang, S.-C. Spin-Orbital Texture in Topological Insulators. *Phys. Rev. Lett.* **2013**, *111*, 066801.

(83) Tamtögl, A.; Kraus, P.; Mayrhofer-Reinhartshuber, M.; Benedek, G.; Bernasconi, M.; Dragoni, D.; Campi, D.; Ernst, W. E. Statics and dynamics of multivalley charge density waves in Sb (111). *NPJ. Quantum Materials* **2019**, *4*, 28.

(84) Li, Y.; Parsons, C.; Ramakrishna, S.; Dwivedi, A.; Schofield, M.; Reyes, A.; Guptasarma, P. Charge Density Wave Order in the Topological Insulator Bi2Se3. *arXiv*: 2002.12546.

(85) Boulfelfel, S. E.; Seifert, G.; Grin, Y.; Leoni, S. Squeezing lone pairs: The A17 to A7 pressure-induced phase transition in black phosphorus. *Phys. Rev. B: Condens. Matter Mater. Phys.* **2012**, *85*, 014110.

(86) Zhang, X.; Stevanovic, V.; d'Avezac, M.; Lany, S.; Zunger, A. Prediction of A$_2$BX$_4$ metal-chalcogenide compounds via first-

principles thermodynamics. *Phys. Rev. B: Condens. Matter Mater. Phys.* **2012**, *86*, 014109.

(87) Zunger, A. Systematization of the stable crystal structure of all AB-type binary compounds: A pseudopotential orbital-radii approach. *Phys. Rev. B: Condens. Matter Mater. Phys.* **1980**, *22*, 5839.

(88) Manjón, F. J.; Vilaplana, R.; Gomis, O.; Pérez-González, E.; Santamaría-Pérez, D.; Marín-Borrás, V.; Segura, A.; González, J.; Rodríguez-Hernández, P.; Muñoz, A.; Drasar, C.; Kucek, V.; Muñoz-Sanjosé, V. High pressure studies of topological insulators $Bi_2Se_3$, $Bi_2Te_3$, and $Sb_2Te_3$. *Phys. Status Solidi B* **2013**, *250*, 669.

(89) Kolobov, A. V.; Haines, J.; Pradel, A.; Ribes, M.; Fons, P.; Tominaga, J.; Katayama, Y.; Hammouda, T.; Uruga, T. Pressure-Induced Site-Selective Disordering of $Ge_2Sb_2Te_5$: A New Insight into Phase-Change Optical Recording. *Phys. Rev. Lett.* **2006**, *97*, 035701.

(90) Arora, A. K. Pressure-induced amorphization versus decomposition. *Solid State Commun.* **2000**, *115*, 665.

(91) Bassett, W. A.; Ming, L.-C. Disproportionation of $Fe_2SiO_4$ to $2FeO+SiO_2$ at pressures up to 250 kbar and temperatures up to 3000 °C. *Phys. Earth Planet. Inter.* **1972**, *6*, 154−160.

(92) Fei, Y.; Mao, H.-K. Static Compression of $Mg(OH)_2$ to 78 GPa at High Temperature and Constraints on the Equation of State of Fluid $H_2O$. *J. Geophys. Res.* **1993**, *98*, 11875−11884.

(93) Kuznetsov, A. Y.; Pereira, A. S.; Shiryaev, A. A.; Haines, J.; Dubrovinsky, L.; Dmitriev, V.; Pattison, P.; Guignot, N. Pressure-Induced Chemical Decomposition and Structural Changes of Boric Acid. *J. Phys. Chem. B* **2006**, *110*, 13858−13865.

(94) Catafesta, J.; Rovani, P. R.; Perottoni, C. A.; Pereira, A. S. Pressure-enhanced decomposition of $Ag_3[Co(CN)_6]$. *J. Phys. Chem. Solids* **2015**, *77*, 151−156.

(95) Duan, D.; Huang, X.; Tian, F.; Li, D.; Yu, H.; Liu, Y.; Ma, Y.; Liu, B.; Cui, T. Pressure-induced decomposition of solid hydrogen sulfide. *Phys. Rev. B: Condens. Matter Mater. Phys.* **2015**, *91*, No. 180502.

(96) Zhu, J.; Zhang, J. L.; Kong, P. P.; Zhang, S. J.; Yu, X. H.; Zhu, J. L.; Liu, Q. Q.; Li, X.; Yu, R. C.; Ahuja, R.; Yang, W. G.; Shen, G. Y.; Mao, H. K.; Weng, H. M.; Dai, X.; Fang, Z.; Zhao, Y. S.; Jin, C. Q. Superconductivity in Topological Insulator $Sb_2Te_3$ Induced by Pressure. *Sci. Rep.* **2013**, *3*, 2016.

(97) Zhao, L.; Deng, H.; Korzhovska, I.; Begliarbekov, M.; Chen, Z.; Andrade, E.; Rosenthal, E.; Pasupathy, A.; Oganesyan, V.; Krusin-Elbaum, L. Emergent surface superconductivity in the topological insulator $Sb_2Te_3$. *Nat. Commun.* **2015**, *6*, 8279.

(98) Kroumova, E.; Aroyo, M. I.; Perez Mato, J. M.; Kirov, A.; Capillas, C.; Ivantchev, S.; Wondratschek, H. Bilbao Crystallographic Server: Useful Databases and Tools for Phase Transitions Studies. *Phase Transitions* **2003**, *76*, 155−170.

(99) Canepa, P.; Hanson, R. M.; Ugliengo, P.; Alfredsson, M. J-ICE: A New Jmol Interface for Handling and Visualizing Crystallographic and Electronic Properties. *J. Appl. Crystallogr.* **2011**, *44*, 225−229.

(100) Marini, C.; Chermisi, D.; Lavagnini, M.; Di Castro, D.; Petrillo, C.; Degiorgi, L.; Scandolo, S.; Postorino, P. High pressure phases of crystalline tellurium: A combined Raman and ab initio study. *Phys. Rev. B: Condens. Matter Mater. Phys.* **2012**, *86*, 064103.

(101) Vilaplana, R.; Gomis, O.; Pérez-González, E.; Ortiz, H. M.; Manjón, F. J.; Rodríguez-Hernández, P.; Muñoz, A.; Errandonea, D.; Lopez-Solano, J.; Ursaki, V. V.; Tiginyanu, I. M. Lattice dynamics study of HgGa2Se4 at high pressures. *J. Phys. Chem. C* **2013**, *117*, 15773−15781.

(102) Ribeiro, G. A. S.; Paulatto, L.; Bianco, R.; Errea, I.; Mauri, F.; Calandra, M. Strong anharmonicity in the phonon spectra of PbTe and SnTe from first principles. *Phys. Rev. B: Condens. Matter Mater. Phys.* **2018**, *97*, 014306.

(103) Pellicer-Porres, J.; Segura, A.; Ferrer-Roca, Ch.; Sans, J. A.; Dumas, P. Investigation of lattice dynamical and dielectric properties of MgO under high pressure by means of mid- and far-infrared spectroscopy. *J. Phys.: Condens. Matter* **2013**, *25*, 505902.

(104) Wang, C.-H.; Jing, X.-P.; Feng, W.; Lu, J. Assignment of Raman-active vibrational modes of $MgTiO_3$. *J. Appl. Phys.* **2008**, *104*, 034112.

(105) Zhao, K.; Wang, Y.; Sui, Y.; Xin, C.; Wang, X.; Wang, Y.; Liu, Z.; Li, B. First principles study of isostructural phase transition in $Sb_2Te_3$ under high pressure. *Phys. Status Solidi RRL* **2015**, *9*, 379−383.

(106) Wang, B.-T.; Souvatzis, P.; Eriksson, O.; Zhang, P. Lattice dynamics and chemical bonding in $Sb_2Te_3$ from first-principles calculations. *J. Chem. Phys.* **2015**, *142*, 174702.

(107) Cardona, M.; Thewalt, M. L. Isotope effects on the optical spectra of semiconductors. *Rev. Mod. Phys.* **2005**, *77*, 1173−1224.

(108) Manjón, F. J.; Serrano, J.; Loa, I.; Syassen, K.; Lin, C. T.; Cardona, M. Effect of Pressure on the Anomalous Raman Spectrum of CuBr. *Phys. Status Solidi B* **2001**, *223*, 331−336.

(109) Krauzman, M.; Pick, R. M.; Poulet, H.; Hamel, G.; Prevot, B. Raman Detection of one-Phonon —Two-Phonon Interactions in CuCl. *Phys. Rev. Lett.* **1974**, *33*, 528−530.

(110) Kanellis, G.; Kress, W.; Bilz, H. Fermi Resonance in the Phonon Spectra of Copper Halides. *Phys. Rev. Lett.* **1986**, *56*, 938−940.

(111) Agranovich, V. M. *Spectroscopy and Excitation Dynamics of Condensed Moiecular Systems*; North-Holland: Amsterdam, 1983; p 83.

(112) Singh, R. K.; Gupta, D. C. Phase transition and high-pressure elastic behavior of copper halides. *Phys. Rev. B: Condens. Matter Mater. Phys.* **1989**, *40*, 11278−11283.

(113) Gopakumar, A.; Gupta, M. K.; Mittal, R.; Rols, S.; Chaplot, S. L. Investigating Anomalous Thermal Expansion of Copper Halides by Inelastic Neutron Scattering and Ab-inito Phonon Calculations. *Phys. Chem. Chem. Phys.* **2017**, *19*, 12107−12116.

(114) Hakeem, M. A.; Jackson, D. E.; Hamlin, J. J.; Errandonea, D.; Proctor, J. E.; Bettinelli, M. High Pressure Raman, Optical Absorption, and Resistivity Study of $SrCrO_4$. *Inorg. Chem.* **2018**, *57*, 7550−7557.

(115) Sakai, N.; Kajiwara, T.; Takemura, K.; Minomura, S.; Fujii, Y. Pressure-induced Phase Transition in $Sb_2Te_3$. *Solid State Commun.* **1981**, *40*, 1045.

(116) Errandonea, D.; Segura, A.; Martínez-García, D.; Muñoz-San Jose, V. Hall-effect and resistivity measurements in CdTe and ZnTe at high pressure: Electronic structure of impurities in the zinc-blende phase and the semimetallic or metallic character of the high-pressure phases. *Phys. Rev. B: Condens. Matter Mater. Phys.* **2009**, *79*, 125203.

(117) Reindl, J.; Volker, H.; Breznay, N. P.; Wuttig, M. Persistence of spin memory in a crystalline, insulating phase-change material. *NPJ. Quantum Materials* **2019**, *4*, 57.

(118) Segura, A.; Panchal, V.; Sánchez-Royo, J. F.; Marín-Borrás, V.; Muñoz-Sanjosé, V.; Rodríguez-Hernández, P.; Muñoz, A.; Pérez-González, E.; Manjón, F. J.; González, J. Trapping of three-dimensional electrons and transition to two-dimensional transport in the three-dimensional topological insulator $Bi_2Se_3$ under high pressure. *Phys. Rev. B: Condens. Matter Mater. Phys.* **2012**, *85*, 195139.

(119) Mio, A. M.; Konze, P. M.; Meledin, A.; KüPers, M.; Pohlmann, M.; Kaminski, M.; Dronskowski, R.; Mayer, J.; Wuttig, M. Impact of Bonding on the Stacking Defects in Layered Chalcogenides. *Adv. Funct. Mater.* **2019**, *29*, 1902332.

(120) Noury, S.; Silvi, B.; Gillespie, R. J. Chemical Bonding in Hypervalent Molecules: Is the Octet Rule Relevant? *Inorg. Chem.* **2002**, *41*, 2164−2172.

(121) Scheiner, S.; Lu, J. Halogen, Chalcogen, and Pnicogen Bonding Involving Hypervalent Atoms. *Chem. - Eur. J.* **2018**, *24*, 8167−8177.

(122) Durrant, M. C. A quantitative definition of hypervalency. *Chem. Sci.* **2015**, *6*, 6614−6623.

(123) Braida, B.; Hiberty, P. C. The essential role of charge-shift bonding in hypervalent prototype $XeF_2$. *Nat. Chem.* **2013**, *5*, 417−422.

(124) Lee, T. H.; Elliott, S. R. Chemical bonding in chalcogenides: the concept of multi-centre hyperbonding. *arXiv* 1909.05281.

(125) Shaik, S.; Danovich, D.; Galbraith, J. M.; Braïda, B.; Wu, W.; Hiberty, P. C. Charge-Shift Bonding: A New and Unique Form of Bonding. *Angew. Chem., Int. Ed.* **2020**, *59*, 984−1001.

(126) Berski, S.; Durlak, P. Dimeric nature of N-coordinated Mg and Ca ions in metaloorganic compounds. The topological analysis of ELF functions for Mg−Mg and Ca−Ca bonds. *Polyhedron* **2017**, *129*, 22−29.

(127) Gatti, C. Chemical bonding in crystals: new directions. *Z. Kristallogr. - Cryst. Mater.* **2005**, *220*, 390−457.

(128) Gaspard, J.-P.; Ceolin, R. Hume-Rothery rule in V-VI compounds. *Solid State Commun.* **1992**, *84*, 839−842.

(129) Sa, B. S.; Miao, N. H.; Zhou, J.; Sun, Z. M.; Ahuja, R. Ab initio study of the structure and chemical bonding of stable $Ge_3Sb_2Te_6$. *Phys. Chem. Chem. Phys.* **2010**, *12*, 1585−1588.

(130) Sans, J. A.; Manjón, F. J.; Pereira, A. L. J.; Vilaplana, R.; Gomis, O.; Segura, A.; Muñoz, A.; Rodríguez-Hernández, P.; Popescu, C.; Drasar, C.; Ruleova, P. Structural, vibrational, and electrical study of compressed BiTeBr. *Phys. Rev. B: Condens. Matter Mater. Phys.* **2016**, *93*, 024110.

(131) Xu, M.; Jakobs, S.; Mazzarello, R.; Cho, J.-Y.; Yang, Z.; Hollermann, H.; Shang, D.; Miao, X. S.; Yu, Z. H.; Wang, L.; Wuttig, M. Impact of Pressure on the Resonant Bonding in Chalcogenides. *J. Phys. Chem. C* **2017**, *121*, 25447.

(132) Cuenca-Gotor, V. P.; Sans, J. A.; Gomis, O.; Mujica, A.; Radescu, S.; Muñoz, A.; Rodríguez-Hernández, P.; da Silva, E. L.; Popescu, C.; Ibáñez, J.; Vilaplana, R.; Manjón, F. J. Orpiment under compression: metavalent bonding at high pressure. *Phys. Chem. Chem. Phys.* **2020**, *22*, 3352−3369.

(133) Matsunaga, T.; Yamada, N. Structural investigation of $GeSb_2Te_4$: A high-speed phase-change material. *Phys. Rev. B: Condens. Matter Mater. Phys.* **2004**, *69*, 104111.

(134) Karpinskii, O. G.; Shelimova, L. E.; Kretova, M. A. Crystal structure and point defects of $Ge_{1+delta}Bi_2Te_4$. *Inorg. Mater.* **1997**, *33*, 793−797.

(135) Shelimova, L. E.; Karpinskii, O. G.; Svechnikova, T. E.; Nikhezina, I. Y.; Avilov, E. S.; Kretova, M. A.; Zemskov, V. S. Effect of cadmium, silver and tellurium doping on the properties of single crystals of the layered compounds $PbBi_4Te_7$ and $PbSb_2Te_4$. *Neorg. Mater.* **2008**, *44*, 438−442.

(136) Agaev, K. A.; Semiletov, S. A. Electron-diffraction study of the structure of $PbBi_2Se_4$. *Kristallografiya* **1968**, *13*, 258−260.